

1 Validation of Rainfall Data Observed by Using Disdrometer under 2 Wet-Bulb Temperature Conditions

3 Hyeon-Joon Kim¹, Sung-Ho Suh², Jongyun Byun³, Changhyun Jun⁴

4 ¹Center of Oceanic and Meteorological Information, Pukyong National University, Busan, South Korea

5 ²Flight Safety Technology Division, NARO Space Center, Korea Aerospace Research Institute, Goheung, South Korea

6 ³Department of Civil, Environmental and Architectural Engineering, Korea University, Seoul, South Korea

7 ⁴School of Civil, Environmental and Architectural Engineering, Korea University, Seoul, South Korea

8

9 *Correspondence to:* Changhyun Jun (cjun@korea.ac.kr)

10 **Abstract.** This study focuses on the reliability assessment of precipitation data calculated from drop size distribution (DSD)
11 based on disdrometer data observations according to wet-bulb temperature (T_w). Three distinct quality control (QC) methods
12 based on fall velocity were implemented and validated against measurements from tipping-buckets and weighing rain gauges
13 collected from January 2020 to February 2024. The analysis indicated that all QC methods exhibited high reliability
14 (correlation coefficient (CC) > 0.98) for rainfall conditions when T_w was above 5 °C, with a mean absolute percentage error
15 (MAPE) of approximately 8.5%. However, the precision of precipitation measurements exhibited a notable decline when T_w
16 was below 2 °C, as indicated by a CC of less than 0.6 and MAPE exceeding 30%. This reduction in accuracy can primarily
17 be attributed to the outcomes of the QC methods, which rely on the falling velocity, given that raindrops and solid particles
18 were observed within the specified T_w range. When considering the melting of snow particles at T_w ranging from 0 °C to 2 °C,
19 the CC approached 0.9, suggesting enhanced measurement reliability. The findings of this study indicate that T_w is a more
20 effective variable than air temperature (T_{air}) for differentiating the precipitation types. This conclusion arises from the
21 observation that the fall velocity of hydrometeors does not reach the terminal velocity of raindrops, even within the T_{air} range
22 of 1–5 °C, coupled with the broad distribution of fall velocities. The DSD shape demonstrated stability across multiple QC
23 methods when T_w was equal to or greater than 2 °C. In contrast, considerable variations were observed at lower temperatures,
24 where particles with diameters ranging from 1 to 2 mm exhibited irregular distribution patterns at temperatures below 1 °C.
25 These results suggest that DSD parameters should be derived from disdrometer data obtained under conditions where T_w is
26 above 2 °C to ensure the reliability of the findings. This study provides critical insights for improving precipitation
27 measurement techniques and DSD analyses in regions with variable temperature conditions.

28 **1 Introduction**

29 Several factors influence the variability in precipitation development, including atmospheric water vapor content, vertical
30 airflow intensity, and temperature and humidity distributions in the vertical profile (Lintner et al., 2017; Padullés et al.,
31 2022). These factors can be categorized as climatological, geographical, or topographical. Climatological factors include
32 alterations in atmospheric water vapor resulting from long-term temperature changes, developmental shifts associated with
33 temperature variations in the upper and lower atmospheric layers, and thermodynamic effects linked to changes in land cover
34 based on climatic characteristics.~~Climatological factors include alterations in atmospheric water vapor resulting from long-~~
35 ~~term temperature changes, developmental shifts associated with temperature variations in the upper and lower atmospheric~~
36 ~~layers, and thermodynamic effects linked to changes in land cover based on climatic characteristics.~~ (Dahlström, 2021; Lu et
37 al., 2024). Geographical and topographical factors include the convergence of water vapor due to mountainous terrain, which
38 facilitates vertical precipitation development (Insel et al., 2010; Lee et al., 2014; Kim et al., 2019), and the generation of
39 vertical flow resulting from increased friction at low levels due to coastal topography (Du and Chen, 2019; Yao et al., 2021).
40 Additionally, precipitation development can be influenced by the temperature differential between the sea and air,
41 particularly when cold air from inland regions moves over water bodies during winter (Steenhurgh, 2020). Various
42 environmental factors can influence the disparities in warm precipitation processes, such as collision-coalescence,
43 evaporation, and accretion, which are contingent upon the vertical development of precipitation types, including stratiform,
44 convective, and typhoon-related precipitation. Similarly, cold precipitation processes such as snow riming, melting, and ice
45 crystal growth are affected by these environmental variables. These factors contribute to the development of diverse
46 hydrometeors including rain, snow, and graupel, which are influenced by temperature variations (Maheskumar et al., 2018;
47 Yi et al., 2021). Environmental factors that influence precipitation development exert both hydrodynamic effects, including
48 variations in lower-level vertical flow and atmospheric convergence or divergence, and thermodynamic effects, such as
49 increased atmospheric instability resulting from water vapor inflow and differences in vertical temperature distribution. The
50 differences in the development of precipitation due to environmental influences from the perspectives of atmospheric
51 dynamics and thermodynamics ultimately lead to variations in the total precipitation observed at the surface. Therefore, it is
52 crucial to acquire data that accurately reflects the microphysical characteristics of precipitation to enhance precipitation
53 monitoring. Furthermore, analyses based on long-term observational data are essential to identify the universal
54 characteristics that account for the temporal variability of precipitation.
55 ~~The differences in the precipitation development processes ultimately lead to variations in the total precipitation observed at~~
56 ~~the surface. Therefore, it is crucial to acquire data that accurately reflects the microphysical characteristics of precipitation to~~
57 ~~enhance precipitation monitoring. Furthermore, analyses based on long-term observational data are essential to identify the~~
58 ~~universal characteristics that account for the temporal variability of precipitation.~~
59 The standard instruments used to observe precipitation include rain gauges and disdrometers. A rain gauge measures the total
60 precipitation accumulated over a specified time interval. In contrast, a disdrometer assesses the size and concentration of

61 precipitation particles, thereby enabling the determination of the precipitation intensity and type. The selection of an
62 appropriate type of rain gauge is contingent on specific observational objectives such as monitoring heavy rain, light rain, or
63 snow. Notable examples of disdrometers include the Particle Size and Velocity (PARSIVEL), Two-dimensional Video
64 Disdrometer (2DVD), Joss-Waldvogel Disdrometer, and Precipitation Occurrence Sensor System. Disdrometers compute the
65 size-specific concentration of particles, known as the Drop Size Distribution (DSD), by analyzing the variations in optical
66 intensity as the particles traverse the observation zone of the sensor. In contrast to data obtained from rain gauges,
67 disdrometer data offer a broader range of applications because they provide physical parameters, such as particle number
68 concentration and fall velocity, and morphological characteristics, such as oblateness.

69 A typical application of disdrometer data involves formulating Quantitative Precipitation Estimation (QPE) equations, which
70 are used in conjunction with remote sensing data such as radar observations. To derive rainfall information from remote
71 sensing data, researchers can leverage the correlation between rain rate and radar reflectivity values, an observational
72 variable in remote sensing, to measure variations in rainfall (Ji et al., 2019; Tang et al., 2024). Additionally, DSD
73 information obtained from disdrometer observations is instrumental in parameterizing microphysical schemes within
74 numerical weather prediction models (Yang et al., 2019; Iversen et al., 2021). Microphysical schemes can be categorized
75 into bin and bulk types (Hu and Igel, 2023). The bin scheme accurately simulates the distributional differences between
76 hydrometeor types by accounting for their size-dependent number concentration. However, this approach is limited by its
77 high computational demand and the need for substantial hardware resources during the simulation process. Consequently,
78 bulk schemes are predominantly employed in weather prediction models. This approach simulates microphysical processes
79 based on the relationships between particle diameter and concentration distributions for various hydrometeor types. The
80 DSD model considerably influences the quantitative differences in the estimated precipitation property outcomes. As the
81 reliability of the DSD model improves, so does the accuracy of the precipitation simulation and forecasting.

82 The DSD model used in the QPE and microphysical schemes of remote sensing encompasses various models, such as the
83 Marshall-Palmer, exponential (Marshall and Palmer, 1948), and gamma models (Ulbrich, 1983). The configuration of each
84 model is contingent on the specific parameters being analyzed, with the shape and slope variables in the DSD model varying
85 according to the concentration distribution based on the particle diameter (Smith, 2003; Liu et al., 2021). The DSD is
86 affected by several factors, such as the type of rainfall (Deo and Walsh, 2016), intensity of rainfall (Thomas et al., 2021), and
87 climatological and topographical characteristics of the region where precipitation occurs and develops (Kim et al., 2022).
88 Consequently, it is imperative to acquire DSD model parameters and reflectivity data by collecting highly reliable
89 observational data that accurately represent precipitation characteristics to enhance the precision of rainfall estimations and
90 simulations based on DSD. Furthermore, disdrometer data can be used to estimate rainfall erosivity (Serio et al., 2019).
91 Enhancing the accuracy of rainfall erosivity estimates can facilitate the assessment of the impact of rainfall on soil erosion
92 and serve as a foundation for developing countermeasures through spatial analysis and monitoring of soil erosion risk areas
93 using remote sensing data. Reliable precipitation observational data for estimating rainfall erosivity can aid in analyzing the
94 effects of erosion resulting from alterations in rainfall patterns due to climate change.

95 Various quality control (QC) methods for disdrometer data have been suggested to enhance the accuracy of derived
96 measurements (Kruger and Krajewski, 2002; Jaffrain and Berne, 2011; Raupach et al., 2015). QC approaches for
97 disdrometer data primarily rely on the falling velocity of raindrops. In the absence of a substantial wind influence or particle
98 collisions during descent, the fall velocity of a raindrop tends to increase with its diameter, ultimately reaching a terminal
99 velocity. Terminal velocity is achieved when the forces of air resistance and gravitational pull are in equilibrium, resulting in
100 no further particle acceleration (Wang and Pruppacher, 1977; Ong et al., 2021). Studies have been conducted to determine
101 the terminal velocities of raindrop particles (Atlas et al., 1973; Beard, 1977; Brandes et al., 2002), which have led to the
102 development of QC methods that use terminal velocity measurements. Kruger and Krajewski (2002) elucidated the structural
103 design and operational principles of a 2DVD system, and noted that the recorded data indicated a fall velocity of
104 approximately 400 m s^{-1} . However, this value is not feasible for raindrops. To mitigate the impact of erroneous data (outliers)
105 potentially arising from hardware malfunctions, inaccuracies in data processing, and environmental conditions at the
106 observation site, we employed a comparative analysis of the empirical relationship of raindrops established by Atlas et al.
107 (1973). Furthermore, recognizing that the disdrometer may either underestimate or overestimate the fall velocity of
108 precipitation particles influenced by the horizontal movement due to wind, this study conducted QC by focusing exclusively
109 on the vertical velocity measurements. Jaffrain and Berne (2011) conducted a study to address the uncertainties associated
110 with sampling observations from PARSIVEL disdrometers. They argued that the collected precipitation data exhibit inherent
111 variability and measurement errors attributable to the equipment used, necessitating the development of a method to mitigate
112 these issues and enhance data reliability. The authors proposed a method for eliminating anomalous data, such as outliers
113 (values that are not physically plausible), instances of particle splashing (where the same particle is detected multiple times),
114 and non-meteorological data. This preprocessing approach effectively diminished the sampling uncertainty of various
115 parameters, including rain rate.

116 Raupach et al. (2015) conducted a study using data from the PARSIVEL and 2DVD to establish a correction factor for
117 number concentration based on observations from the PARSIVEL disdrometer. The authors noted a tendency for
118 PARSIVEL to overestimate the number of small droplets measuring between 0.2 and 0.4 mm and larger particles measuring
119 2.4 mm or more. Furthermore, the measured fall velocity of larger droplets was lower than the actual terminal velocity.
120 Anomalous data can lead to DSD distortions, which can compromise the accuracy of precipitation measurements and radar-
121 based rainfall estimates. The focus of these studies was primarily on rainfall particles and it was determined that the
122 quantitative accuracy of rainfall estimates improved when the aforementioned QC methods were applied across various
123 environmental conditions.

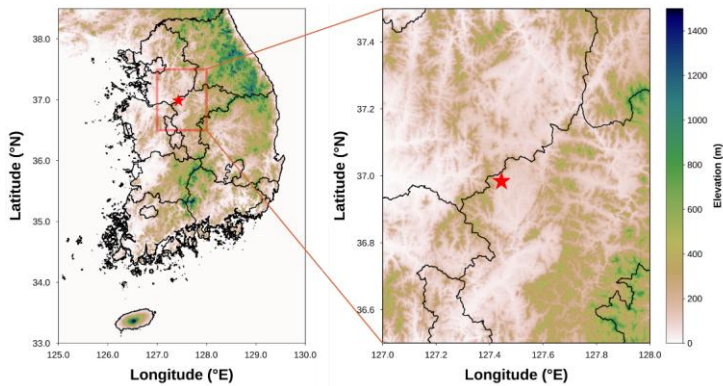
124 Snow particles exhibit a variety of forms such as needles, dendrites, and granules, which are influenced by temperature and
125 humidity. These variations in shape arise from the specific conditions under which the particles form and develop, leading to
126 differences in their densities and fall velocities (Barthazy and Schefold, 2006; Vázquez-Martín et al., 2021). Furthermore,
127 snow particles are more susceptible to wind because of their lower density and larger surface area than raindrops.
128 Consequently, fall-velocity-based QC methods for eliminating non-meteorological particles (such as leaves, dust, and insects)

129 are limited in their effectiveness because they primarily target solid particles with low fall velocities. Given the diverse
130 shapes and fall speeds of snow particles, the mixing of raindrops and snow during precipitation events may lead to an
131 underestimation of errors when applying conventional disdrometer QC methods. Therefore, it is imperative to establish
132 objective criteria for differentiating rainfall and snowfall conditions to enhance the accuracy of rainfall analysis using
133 disdrometer data. Ding et al. (2014) emphasized the significance of accurately classifying precipitation types for surface
134 energy balance and hydrological process research. They aimed to develop a method for identifying precipitation types by
135 analyzing 30 years of observational data. Their investigation focused on the correlation between precipitation type and
136 various meteorological variables, including wet-bulb temperature (T_w), relative humidity (RH), and surface elevation. These
137 findings indicate that using T_w as a reference variable for determining precipitation type is more reliable than relying on air
138 temperature (T_{air}). Furthermore, the proposed model, which incorporated T_w , demonstrated a determination accuracy
139 exceeding 88%.

140 This study aims to evaluate the quantitative accuracy of rainfall measurements obtained from a disdrometer in relation to
141 varying T_w conditions. Furthermore, this study seeks to establish environmental criteria to ensure the reliability of the
142 parameters used in the DSD model by using long-term rainfall data collected through disdrometer observations. A
143 comparative analysis of the disdrometer data was performed using different QC methods to examine the discrepancies
144 between these methods under varying T_w conditions.

145 **2 Data**

146 In this study, we evaluated the QC method applied to disdrometer data under varying precipitation conditions. To achieve
147 this, we collected and analyzed regional observational data that accounted for the environmental factors associated with
148 rainfall and snowfall. This study used data from a 2DVD installed at an observatory (Fig. 1) operated by the Weather Radar
149 Center of the Korea Meteorological Administration. The integrity of the 2DVD data was corroborated through comparisons
150 with measurements obtained from the tipping-bucket and weighing rain gauges. The analysis included observational data
151 collected between January 2020 and February 2024.



152 **Figure 1: Location of ground observation station.**

153 **2.1 Disdrometer**

154 The 2DVD (Kruger and Krajewski, 2002) used for the validity analysis of the disdrometer was an optical disdrometer
 155 developed by Joanneum Research. This instrument operates by projecting light through a bulb across a designated
 156 observation area and capturing the intensity of the transmitted light using a camera positioned on the opposite side (Fig. 2).
 157 When a particle, such as a raindrop, traverses the observation area (10 cm²) illuminated by the light sheet, its diameter is
 158 determined by analyzing the reduction in the intensity and width of the light during its passage. Furthermore, the system
 159 employs two cameras to observe the particles from orthogonal angles, allowing the fall velocity to be calculated based on the
 160 differential height of the light sheet in the two orientations and time taken for the particles to descend. The 2DVD's
 161 capability to acquire diameter and fall velocity data for individual particles offers superior temporal, dimensional, and
 162 velocity resolution compared to traditional disdrometer data, which typically provide channel-based information. The
 163 observational resolution of the camera was approximately 0.2 mm (512 pixels), making the particles smaller than the
 164 indistinguishable threshold (Grazioli et al., 2014). For quantitative validation using rain gauge data, the output time
 165 resolution was configured to one minute, with data classified at one-minute intervals.



166 **Figure 2: Two-dimensional video disdrometer.**

167 **2.2 Rain gauge**

168 Precipitation can occur in liquid droplets and solid particles, such as snow and graupel, when temperatures are at or near 0 °C.
 169 To validate the disdrometer data under T_w conditions, an analysis was conducted using data from the tipping-bucket and
 170 weighing-type rain gauges (Fig. 3). Each type of rain gauge offers an observational resolution of 0.1 mm and a temporal
 171 resolution of 1 min. Both instruments were positioned within a 10 m radius of the 2DVD disdrometer.

(a) Tipping-bucket type



(b) Weighing type



172 **Figure 3: (a) Tipping-bucket rain gauge (0.1 mm) and (b) Weighing rain gauge (0.1 mm).**

173 3 Methods

174 Ding et al. (2014) argued that precipitation types such as rain, snow, and sleet co-occur when the T_{air} or T_w approaches or
175 falls below 0 °C. They recommended using T_w as a more effective criterion for distinguishing between types of precipitation
176 instead of relying solely on T_{air} . In this study, the temporal resolution of the temperature data differed from that of previous
177 studies, which employed different temporal resolutions. To facilitate objective verification of the applicability of T_w , T_{air} and
178 T_w were employed as criteria for classifying precipitation types, and a comprehensive analysis was conducted.

179 3.1 Pre-processing of disdrometer data

180 A common QC approach for disdrometer data involves excluding non-meteorological data by analyzing fall velocity. In
181 numerous studies (Kruger and Krajewski, 2002; Jaffrain and Berne, 2011; Raupach and Berne, 2015; Kim et al., 2019), this
182 QC process was implemented by establishing a threshold determined by the terminal velocity, as indicated in Eq. (1).

$$183 |V_{measured} - V_{ideal}| < C \times V_{ideal} \quad (1)$$

184 where $V_{measured}$ and V_{ideal} represent the observed particle fall velocity (in m s^{-1}) and empirical fall velocity (or terminal
185 velocity), respectively. Constant C denotes the setting constant, which indicates the percentage of the terminal velocity. The
186 proportion of the removed particles may fluctuate based on the value of C . Numerous previous studies have provided
187 validation results using various setting constants. Studies that employed 2DVD data (Kruger and Krajewski, 2002; Thurai
188 and Bringi, 2005; Chang et al., 2009; Wen et al., 2018) predominantly adopted a setting constant of 0.4 (40%) during data
189 processing. Studies that employed PARSIVEL data for analysis frequently applied a setting constant of 0.6, accounting for
190 60% of the cases (Jaffrain and Berne, 2011; Friedrich et al., 2013; Ji et al., 2019; Kim et al., 2019). Given that previous
191 studies have encompassed various precipitation types, such as heavy rainfall, typhoons, orographic rainfall, and
192 thunderstorms, the established 40% and 60% QC conditions can be regarded as reliable preprocessing criteria for rainfall

193 Raupach and Berne (2015) used data from a 2DVD instrument to derive correction factors for the drop-diameter channel in
194 the PARSIVEL dataset. The fall velocity filtering technique employed for the 2DVD and PARSIVEL data involved the
195 exclusion of particles exhibiting a terminal velocity exceeding 4 m s^{-1} , as shown in Eq. (2), those with a fall velocity below 3
196 m s^{-1} , as indicated in Eq. (3), and those larger than 7.5 mm , as shown in Eq. (4).

$$V_{measured} > V_{ideal} + 4 \quad (2)$$

$$V_{measured} > V_{ideal} - 3 \quad (3)$$

$$D > 7.5 \quad (4)$$

197 where D (in mm) is the diameter of the drop (or particle). This study involved a comparative analysis of the outcomes
198 derived from the three QC methods based on fall velocity. Terminal velocity was determined using the equation established
199 by Atlas et al. (1973) (Eq. (5)).

$$V_{ideal}(D) = 9.65 - 10.3\exp(-0.6D) \quad (5)$$

200 Three QC methods were used to evaluate the research findings. Methods 1 and 2 are used for the $\pm 40\%$ and $\pm 60\%$ ranges of
 201 terminal velocity, respectively, whereas Method 3 is based on the approach proposed by Raupach and Berne (2015).
 202 As the temperature decreased, various hydrometeors intermingled, resulting in a gradual reduction in the proportion of
 203 raindrops. Current QC methods are capable of eliminating low-density snow particles; however, to quantitatively compare
 204 and validate rainfall measurements obtained from rain gauge observations, particles that exhibit velocities below the
 205 threshold established for raindrops in each QC method are categorized as solid meteorological particles. In addition, analyses
 206 were conducted under the assumption that the solid particles melted and transformed into raindrops. This method aims to
 207 evaluate data from tipping-bucket rain gauges, which may exhibit diminished quantitative accuracy as the proportion of solid
 208 particles increases, and facilitate quantitative comparisons of rainfall observations derived from disdrometer data by
 209 implementing the QC method as the temperature decreases.

210 The equivalent-melted diameter (D_{eq}) at which a snow particle can transition into a raindrop while preserving its mass was
 211 determined using Eq. (6), established by Delanoë et al. (2005). In this equation, $\rho(D)$ (g cm^{-3}) denotes the density of snow
 212 particles as a function of their diameter, while ρ_w (g cm^{-3}) denotes the density of water. The density of the snow particles was
 213 computed based on the formula provided by Tiira et al. (2016) (Eq. (7)).

$$D_{eq} = \left(\rho(D) / \rho_w \right)^{1/3} D \quad (6)$$

$$\rho(D) = 0.226D^{-1.004} \quad (7)$$

214 3.2 Raindrop size distribution

215 The 2DVD data can be configured to correspond to user-defined diameter bin sizes, which in turn influence the
 216 characteristics of the DSD output and the precision of the DSD model parameters (Marzuki et al., 2010). Consequently, this
 217 study aims to facilitate the analysis of PASIVEL and 2DVD data for comparative purposes. To achieve this, 2DVD data
 218 were processed using the diameter channel information derived from the PASIVEL data to compute the rain rate, number
 219 concentration, and DSD model parameters. Detailed information regarding the diameter and velocity channels of the
 220 PASIVEL data is provided in the appendices (Table A13-14). The rain rate (R , mm h^{-1}) is calculated using Eq. (8), which
 221 incorporates the number concentration and fall velocity for each diameter. In determining the DSD model parameters after
 222 the rain rate calculation, data from intervals where the rain rate was 0.1 mm h^{-1} or greater were considered, thereby
 223 minimizing the uncertainty associated with the DSD model. The gamma model, recognized for its reliability in representing
 224 DSD characteristics, was selected for analysis. The gamma model is a widely used DSD model that enables the derivation of
 225 rainfall characteristics by capturing both the flatness and the overall shape of the number concentration distribution. This
 226 model (Eq. (9)) is characterized by the shape parameter μ (Eq. (10)), slope parameter A (mm^{-1}) (Eq. (11)), and intercept
 227 parameter N_0 ($\text{mm}^{-1}\mu\text{m}^{-3}$) (Eq. (12)).~~The gamma model, recognized for its reliability in representing DSD characteristics,~~
 228 ~~was selected for analysis. This model (Eq. (9)) is characterized by the shape parameter μ (Eq. (10)), slope parameter A (mm^{-1})~~
 229 ~~(Eq. (11)), and intercept parameter N_0 ($\text{mm}^{-1}\mu\text{m}^{-3}$) (Eq. (12)).~~

$$R = \frac{6\pi}{10^4} \int_{D_{min}}^{D_{max}} D^3 N(D) V(D) dD \quad (8)$$

$$N(D)_{gamma} = N_0 D^\mu \exp(-\Lambda D) \quad (9)$$

$$\mu = \frac{(7 - 11\eta) - [(7 - 11\eta)^2 - 4(\eta - 1)(30\eta - 12)]^2}{2(\eta - 1)} \quad (10)$$

$$\Lambda = \left[\frac{M_2 \Gamma(\mu + 5)}{M_4 \Gamma(\mu + 3)} \right]^{1/2} = \left[\frac{M_2(\mu + 4)(\mu + 3)}{M_4} \right]^{1/2} \quad (11)$$

$$N_0 = \frac{\Lambda^{(\mu+3)} M_2}{\Gamma(\mu + 3)} \quad (12)$$

230 The DSD parameters were derived from the n^{th} moment (M_n), as indicated in Eq. (13), along with the η value, computed
231 based on M_n as shown in Eq. (14).

$$M_n = \int_{D_{min}}^{D_{max}} D^n N(D) dD \quad (13)$$

$$\eta = \frac{\langle M_4 \rangle^2}{\langle M_2 \rangle \langle M_6 \rangle} = \frac{(\mu + 3)(\mu + 4)}{(\mu + 5)(\mu + 6)} \quad (14)$$

232 3.3 Wet-bulb temperature

233 Data from an Automatic Weather Station (AWS) installed at the observatory were used to compute the T_w . The T_{air} (in
234 degrees Celsius) and RH (in percentages) values derived from the AWS observations were incorporated into the T_w (in
235 degrees Celsius) calculation equation proposed by Stull (2011) (Eq. (15)) to determine the T_w value. The term "atan" in Eq.
236 (15) denotes the inverse tangent function. The temporal resolution of RH , T_{air} , and T_w was one minute, which was consistent
237 with the temporal resolution of the disdrometer data.

$$T_w = T_{air} \operatorname{atan}\left[0.151977(RH + 8.313659)^{1/2}\right] + \operatorname{atan}(T_{air} + RH) - \operatorname{atan}(RH - 1.676331) \quad (15)$$

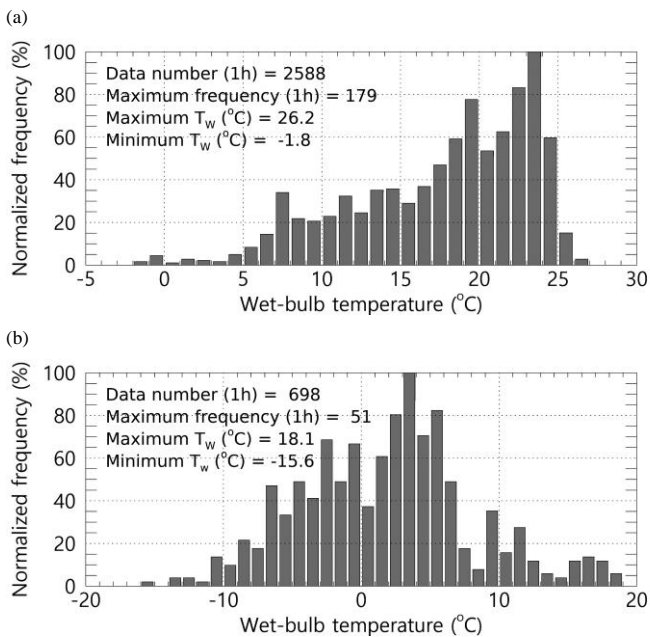
$$+ 0.00391838(RH)^{\frac{3}{2}} \operatorname{atan}(0.023101RH) - 4.686035$$

238 4 Results

239 4.1 Comparison of rainfall by the disdrometer pre-processing method

240 To validate the three QC methods employed for the disdrometer in this study, a comparative analysis was conducted between
241 the rainfall measurements obtained from the disdrometer and those recorded by rain gauges. This comparison utilizes hourly
242 accumulated rainfall data. Given that the QC methods for the disdrometer were specifically designed to address rainfall, the
243 variable T_w was employed to differentiate between rainfall and snowfall, thereby facilitating the verification of precipitation
244 type. Ding et al. (2014) argued that snow is infrequently detected when T_w exceeds 5 °C. Figure 4 shows the distribution of
245 T_w during the analysis period, specifically for instances when the hourly average T_w was either above or below 5 °C. An

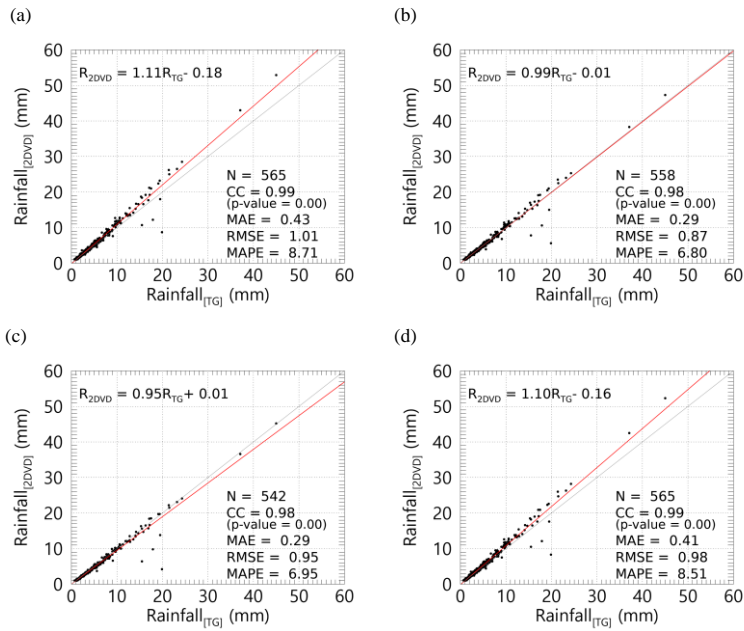
246 examination of the one-minute T_w distribution during periods when the one-hour average T_w was 5 °C or higher (Fig. 4a)
 247 revealed a maximum T_w of 26.2 °C, with the highest proportion of values exceeding 20 °C. Conversely, the proportion of
 248 values falling below 5 °C was minimal, accounting for less than 5%. These findings suggest that it is feasible to delineate
 249 rainfall periods using the hourly average T_w as a reference when comparing hourly accumulated rainfall values. In contrast,
 250 the distribution of one-minute T_w during hours when the average T_w was below 5 °C exhibited a broad range, with minimum
 251 and maximum T_w values exceeding 33 °C and a concentration of T_w values around 0 °C. This observation indicates notable
 252 variability in T_w under 5 °C or lower, suggesting that the observational area encompasses environmental conditions
 253 conducive to detecting diverse hydrometeors.



254 **Figure 4: Normalized frequency distribution of T_w during the analysis period (when the average hourly T_w is (a) $T_w \geq 5$ °C, (b) $T_w <$**
 255 **5 °C).**

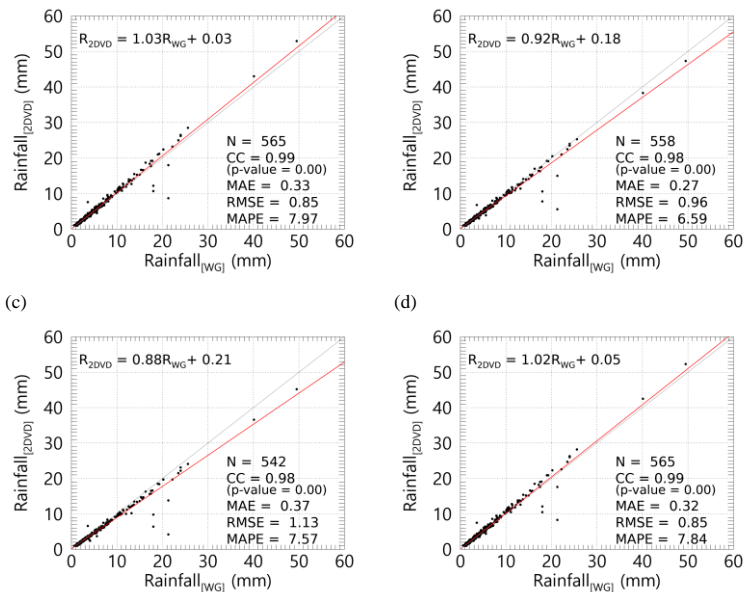
256 Figure 5-6 presents a comparative analysis of hourly rainfall measurements obtained from the tipping-bucket and weighing
 257 rain gauge, specifically under conditions where the temperature (T_w) equals or exceeds 5 °C, alongside data from the 2DVD
 258 observations. The results derived from the unprocessed raw data were analyzed to evaluate the impact of the QC procedures.
 259 The findings indicated a strong correlation, exceeding 0.98, between the 2DVD and rain gauge measurements, with a
 260 regression line slope of approximately unity. However, the raw data tended to overestimate the 2DVD-derived rainfall

261 estimates compared to the QC-processed results. This discrepancy in the overestimation of the 2DVD data can be attributed
 262 to variations in the conditions under which particles are eliminated, which is contingent on the specific QC method
 263 employed. Following the application of the QC methods, the mean absolute percentage error (MAPE) demonstrated an
 264 overall reduction compared with the raw data, suggesting that all QC methods possess quantitative reliability for rainfall data,
 265 with a maximum reduction of approximately 2.1%.



266 Figure 5: Comparison of rainfall observed using the tipping-bucket rain gauge and 2DVD when $T_s \geq 5$ °C ((a) Unfiltered, (b)
 267 Method 1, (c) Method 2, (d) Method 3). R_{2DVD} and R_{TG} denote the rainfall obtained from the 2DVD and a tipping-bucket rain
 268 gauge, respectively.

(a) (b)



269 **Figure 6: Comparison of rainfall observed using the weighing rain gauge and 2DVD when $T_w \geq 5$ °C ((a) Unfiltered, (b) Method 1,**
 270 **(c) Method 2, (d) Method 3). R_{WG} denotes the rainfall obtained from a weighing rain gauge.**

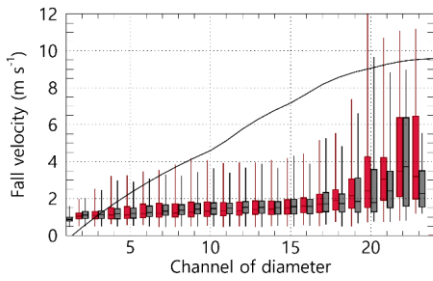
271 4.2 Fall velocity of particle by temperature and wet-bulb temperature

272 4.2.1 Fall velocity distribution at T_{air} and T_w

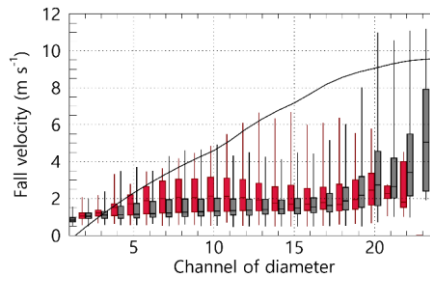
273 Figure 7 shows the distribution of the fall velocity with the diameter of precipitation particles (raindrops) under varying
 274 conditions of T_w and T_{air} . When the T_w and T_{air} ranged from -1 to 0 °C, the fall velocity distributions were relatively
 275 comparable. However, as the temperature exceeded 0 °C, the fall velocity for CH 4 to 18 increased under T_w conditions,
 276 while under the T_{air} condition, it exhibited values similar to those observed at temperatures below 0 °C (Fig. 7(a-b)). When
 277 T_w was below 0 °C, the upper 75% value of fall velocity was less than 2 m s⁻¹. However, as T_w increased above 0 °C, fall
 278 velocity increased to approximately 1 m s⁻¹ or higher in the CH4–15 diameter range. Particularly in the CH8–11 range, the
 279 upper 75% value exceeded 3 m s⁻¹. Specifically, up to CH13, the fall velocity gradually increased with diameter, reaching
 280 large values exceeding 6 m s⁻¹. Conversely, under T_{air} conditions, the upper 75% fall velocity values for the CH1–15 range
 281 were 2 m s⁻¹ or less in the 0–1 °C range. Under T_{air} conditions, the fall velocity increased when the temperature was above
 282 1 °C. Notably, when the temperature rose above 1 °C, there was a notable increase in fall velocity; under T_w conditions, the
 283 distribution approached the terminal velocity of raindrops. Conversely, for diameters in the CH 12 or a higher range, the fall

284 velocity remained at approximately 5.5 m s^{-1} despite increases in diameter. Under T_{air} conditions, the fall velocity increased
 285 when temperatures were above $1 \text{ }^\circ\text{C}$. However, it remained lower than that observed under T_w conditions, with a broader
 286 distribution of fall velocities across the diameter channels (Fig. 7(c)). At $2 \text{ }^\circ\text{C}$ or higher temperatures, T_w and T_{air} conditions
 287 yielded fall velocity distributions that were close to the terminal velocity of raindrops, with an increasing trend in
 288 distribution as temperature increased (Fig. 7(d-f)). However, under T_{air} conditions, the fall velocity was notably low,
 289 remaining below 2 m s^{-1} for diameters of 3 mm (CH 17) or larger.

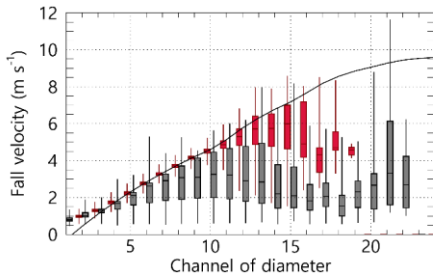
(a) $-1 \text{ }^\circ\text{C} \leq T_w (T_{air}) < 0 \text{ }^\circ\text{C}$



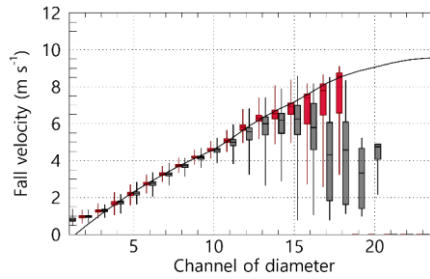
(b) $0 \text{ }^\circ\text{C} \leq T_w (T_{air}) < 1 \text{ }^\circ\text{C}$



(c) $1 \text{ }^\circ\text{C} \leq T_w (T_{air}) < 2 \text{ }^\circ\text{C}$

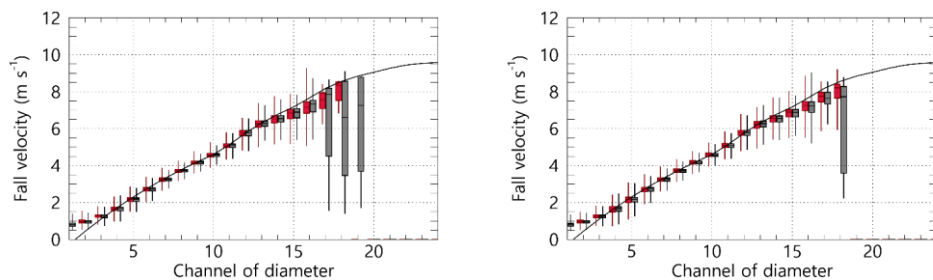


(d) $2 \text{ }^\circ\text{C} \leq T_w (T_{air}) < 3 \text{ }^\circ\text{C}$



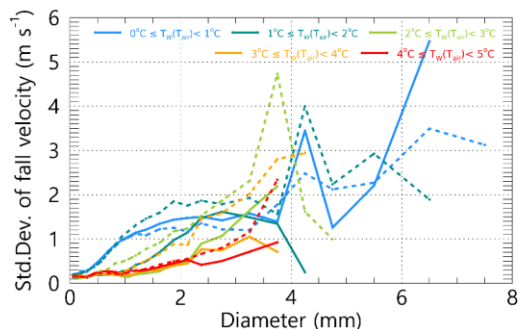
(e) $3 \text{ }^\circ\text{C} \leq T_w (T_{air}) < 4 \text{ }^\circ\text{C}$

(f) $4 \text{ }^\circ\text{C} \leq T_w (T_{air}) < 5 \text{ }^\circ\text{C}$



290 **Figure 7: Distribution of fall velocity by diameter channel based on T_w (red) and T_{air} (gray). The black solid line represents the**
 291 **terminal velocity of rain drops proposed by Atlas et al. (1973).**

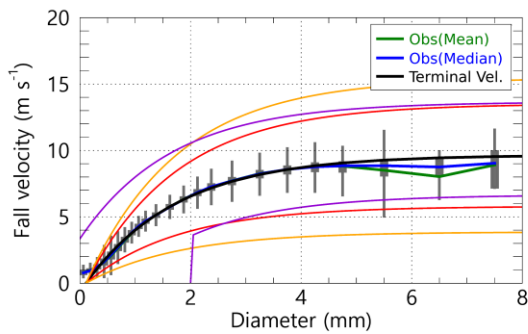
292 Figure 8 shows the variability in fall velocity with respect to the changes in temperature. Notably, despite T_w and T_{air}
 293 exhibiting similar numerical ranges, the distribution of fall velocity was considerably broader under T_{air} conditions. When T_w
 294 exceeds 3 °C, the standard deviation across all diameter intervals remains low, approximately 1 m s⁻¹ or less. In instances
 295 where T_w ranges between 2 and 3 °C, an increase in distribution is observed for diameters of 2.5 mm or greater, while the
 296 standard deviation for diameters of 1 mm or more increases when T_w is between 1 and 2 °C. As temperature decreased, the
 297 range of diameters exhibiting increased fall velocity variability progressively expanded. According to the findings under T_{air}
 298 conditions, the standard deviation of fall velocity for diameters exceeding 1 mm begins to rise below 4 °C, with values
 299 surpassing 1 m s⁻¹ for diameters greater than 2 mm. The observation that when T_{air} is between 2 and 3 °C, the standard
 300 deviation of fall velocity for diameters ranging from 3 to 4 mm is considerably increased, exceeding 2 m s⁻¹ and reaching up
 301 to 4.5 m s⁻¹ is noteworthy. This broad fall velocity distribution suggests a mixture of various hydrometeors, complicating the
 302 differentiation between rain and snow based solely on fall velocity. Consequently, subsequent analyses were conducted
 303 using T_w as the criterion for distinguishing between rain and snow.



304 **Figure 8: Standard deviation of fall velocity by T_w (solid line) and T_{air} (dash line) range (1 °C interval).**

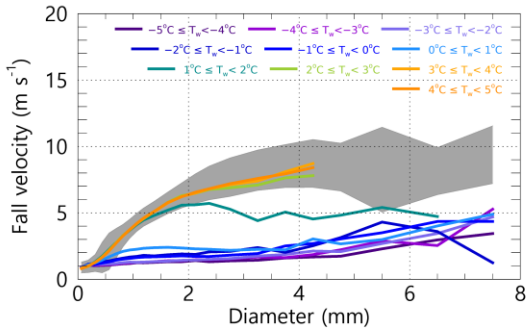
305 **4.2.2 Fall velocity distribution under rainfall condition**

306 Figure 9 shows the distribution of fall velocities by diameter, derived from data collected when the T_w was at or above 5 °C.
307 The central value of the fall velocity is consistent with the terminal velocity. This is within the range of fall velocities for
308 raindrops, as established by the three different QC methods based on the fall velocity. It is important to note that
309 precipitation particles (drops) may experience variations in their fall velocities owing to factors such as wind influence or
310 collisions with obstacles during descent. The findings presented in Fig. 9 suggest that the observatory's measurements were
311 not considerably affected by wind or obstacles, thereby confirming the reliability of the velocity observation data of the
312 disdrometer.



313 **Figure 9: Distribution of fall speed by diameter under conditions of $T_w \geq 5$ °C, and effective fall velocity of raindrops by pre-**
314 **processing methods (The red (method 1), orange (method 2), and purple (method 3) solid lines represent the effective velocity of**
315 **raindrop applied to each QC method).**

316 An analysis of the fall velocity corresponding to temperature intervals (T_w) of 1 °C revealed that when T_w is at or above 2 °C,
317 the fall velocities correspond with those typically observed for raindrops. Conversely, at T_w values between 1°C and 2 °C,
318 particles with diameters of 2 mm or less fall within the raindrop velocity range; however, as the diameter increases to 2 mm
319 or more, the fall velocity diminishes, stabilizing at approximately 5 m s⁻¹. Temperature conditions (T_w) may indicate a
320 mixture of raindrops and snow particles. At temperatures below 1 °C, the fall velocity of droplets with diameters of 4 mm or
321 less decrease to approximately 3 m s⁻¹, exhibiting a low-velocity distribution of 5 m s⁻¹ or less across all diameter ranges.
322 This distribution suggests a higher proportion of solid (snow) particles when T_w is less than 1 °C.



323 **Figure 10: Distribution of fall velocity by diameter in each T_w range. The grey area in the figure represents the Q1 (25%) – Q3**
 324 **(75%) for the fall velocity by diameter when $T_w \geq 5$ °C.**

325 4.3 Accuracy of quantitative rainfall by wet-bulb temperature

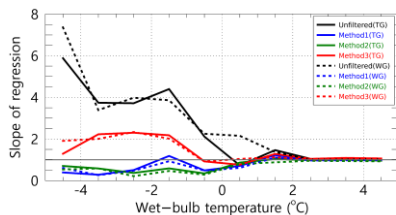
326 Figures 11 and 12 show the outcomes of the comparative analysis and validation of rainfall measurements derived from the
 327 QC method applied to each T_w range, juxtaposed with the rainfall values obtained from a rain gauge. Figure 11 shows the
 328 results of applying the QC method, which effectively filtered out all particles except for raindrops. In contrast, Fig. 12
 329 depicts the assumption that the particles exhibiting low fall velocities are snow that melts and transforms into raindrops. The
 330 verification metrics employed in this analysis included the Root Mean Square Error (RMSE), Mean Absolute Error (MAE),
 331 MAPE, Correlation Coefficient (CC), slope (a_1), and intercept (a_0) derived from Eq. (14), which is the first-order regression
 332 equation correlating rainfall measurements from the rain gauge and 2DVD.

$$R_{2DVD} = a_1 R_{Gauge} + a_0 \quad (14)$$

333 The a_1 of the observed relationship indicates that when the T_w exceeds 2 °C, the value remains close to one before and
 334 following the application of QC. However, as T_w drops below 2 °C, the value of a_1 either increases or decreases. A value of
 335 a_1 greater than one suggests that the rainfall measurements derived from the 2DVD instrument tend to overestimate the
 336 corresponding values obtained from the rain gauge observations. In contrast, a value of less than one indicates an
 337 underestimation. Notably, in the absence of QC, a_1 increases to two or more at temperatures below 0 °C, with the extent of
 338 overestimation intensifying as T_w decreases. This phenomenon is particularly evident when validated against a tipping-
 339 bucket rain gauge, where values of two or greater were recorded at temperatures ranging from 0 to 1 °C. This observation
 340 may be attributed to the different operational principles of the various rain gauge types within the specified T_w range (Fig.
 341 11a). At T_w below 0 °C, the unfiltered data and Method 3 exhibit a_0 values exceeding one, while Method 2 and Method 3
 342 present a_1 values below one. This discrepancy can be interpreted as a consequence of the varying quantities of preprocessed
 343 particles. For T_w values of 1 °C or higher, a_0 is observed to range between 0 and 1; however, as T_w declines below 1 °C, a_0

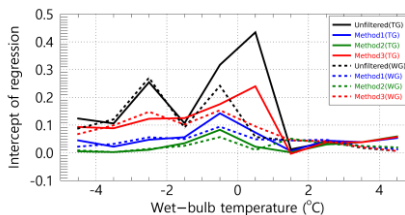
344 experiences a rapid increase. Method 3, which uses a smaller filter area for unfiltered particles and those with diameters of 2
 345 mm or less, demonstrates a_0 values of 0.2 or higher, exceeding those of Methods 1 and 2 (Fig. 11b).
 346 The CC decreases substantially in the T_w range, whereas a_0 increases considerably (Fig. 11f). The RMSE and MAE were
 347 recorded at low values of less than 0.3 mm and 0.2 mm, respectively, when T_w was at or above 2 °C; however, these errors
 348 increased as T_w decreased to 1 °C or lower, with the magnitude of errors following the order of Unfiltered, Method 3,
 349 Method 1, and Method 2, which corresponds to the increasing trend of a_1 . In the range of 0 to 2 °C, the errors associated with
 350 results validated by the tipping-bucket rain gauge were greater than those from the weighing rain gauge (Fig. 11(c-d)). The
 351 MAPE exhibited its lowest error rate, below 20%, at temperatures between 3 and 4 °C. It progressively increased with a
 352 decrease in T_w , ultimately reaching values of approximately 30% or more at temperatures of 2 °C or lower.
 353 Comparable findings were observed when it was assumed that the snow particles melted (Fig. 12), with an increase in error
 354 as the temperature (T_w) dropped below 2 °C. The distinction between melted and unmelted snow particles was demonstrated
 355 using a weighing rain gauge as a verification tool. In scenarios where the melted state was disregarded at T_w values lower
 356 than 2 °C, the variability in the MAPE and CC was substantial, which was contingent upon fluctuations in T_w . Conversely,
 357 the variability decreased when the melted state was considered, and the CC remained elevated approximately at 0.8 or above.
 358 The pronounced escalation in error within the 0–1 °C range can be attributed to precipitation detected by the 2DVD system
 359 that was not captured by the Tipping-bucket rain gauge (Fig. A1(f) in Appendix).
 360 Furthermore, the low volatility and high correlation observed in the verification results using the weighing rain gauge within
 361 the T_w range can be explained by incorporating raindrops and snow particles in the 0–1 °C range. By assuming melting of
 362 snow particles, both forms of precipitation can be integrated into precipitation calculations. The weighing rain gauge
 363 recorded precipitation values that accounted for the cumulative weight of all the raindrops and snow particles (Fig. A2(f) in
 364 the Appendix).

(a) a_1

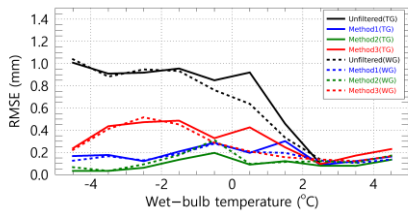


(c) RMSE

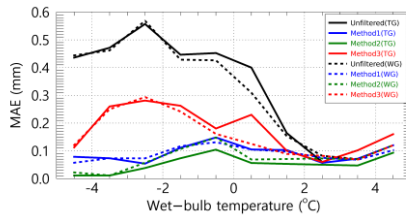
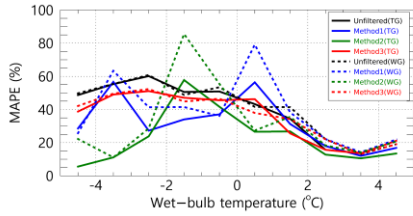
(b) a_0



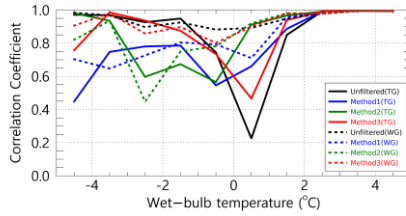
(d) MAE



(e) MAPE

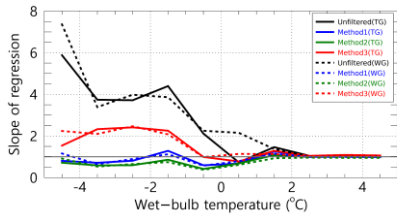


(f) CC

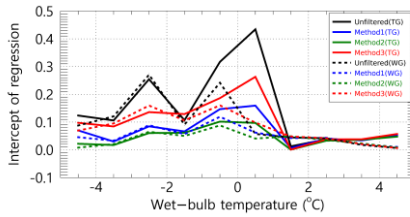


365 **Figure 11: Quantitative comparison of rainfall from a rain gauge (The solid line represents the tipping-bucket and the dash line**
 366 **represents the weighing rain gauge) and 2DVD by T_w (assuming that snow particles do not melt).**

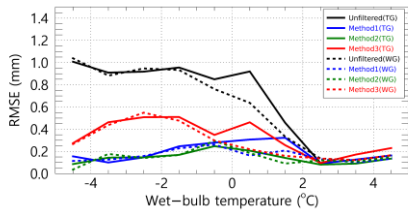
(a) a1



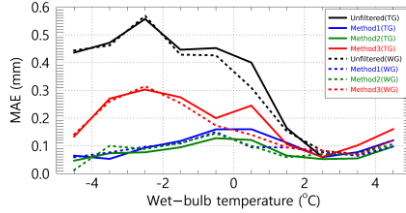
(b) a0



(c) RMSE

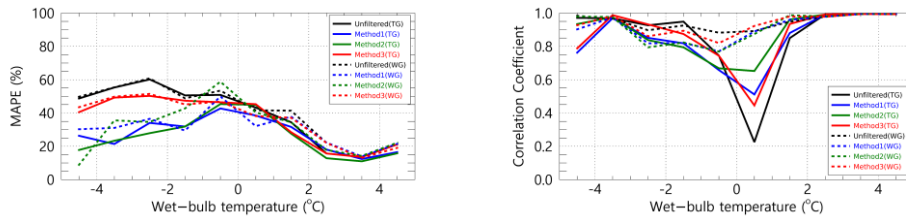


(d) MAE



(e) MAPE

(f) CC

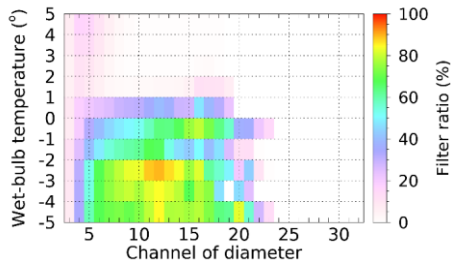


367 **Figure 12: Quantitative comparison of rainfall from a rain gauge (The solid line represents the tipping-bucket and the dash line**
 368 **represents the weighing rain gauge) and 2DVD by T_w (assuming that snow particles melt).**

369 **4.4 Particle filter rate**

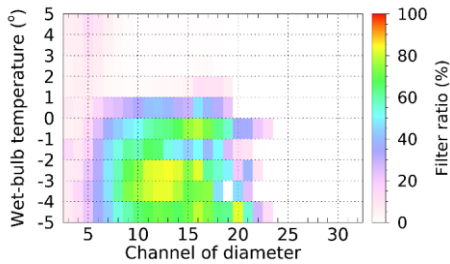
370 Precipitation measurements obtained from the disdrometer were derived from raindrop (or snow particle) accumulation. The
 371 quantitative errors associated with these precipitation measurements were assessed by comparing the filter rates of raindrops
 372 (or snow particles) using the QC method. Figure 13 shows the filter ratios corresponding to the T_w range and channel
 373 diameter. The two methods, Method 1 and Method 2, exhibit differences in the range of removal velocities based on particle
 374 diameter (see Fig. 9); specifically, Method 2 encompasses a broader spectrum of raindrop sizes compared to Method 1,
 375 leading to an increased filter rate when the T_w is below 0 °C. Notably, the filter rate for Method 2 surpasses that of Method 1
 376 at temperatures lower than -2 °C. Conversely, Method 3 did not allow the removal of particles smaller than 2 mm (as
 377 indicated in CH 14), regardless of their low fall velocity, resulting in a consistent filter rate of 0%, irrespective of variations
 378 in T_w . This suggests that the number of particles smaller than 2 mm may be greater in Methods 1 and 2. Furthermore, the
 379 filter rate was lower when snow particles were assumed to have melted than when they had not melted. Nonetheless, for
 380 particles with a diameter of 1 mm or less, the filter rate ranged from approximately 10% to 30% when T_w exceeded 1 °C,
 381 which appears to be attributable to the removal of particles exhibiting a fall velocity that exceeds the raindrops.

(a) Method 1

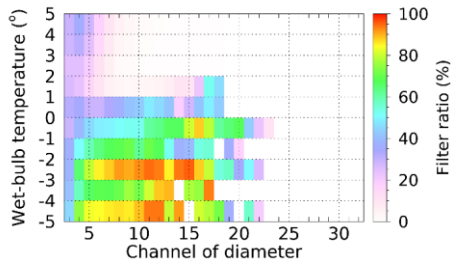


(c) Method 2

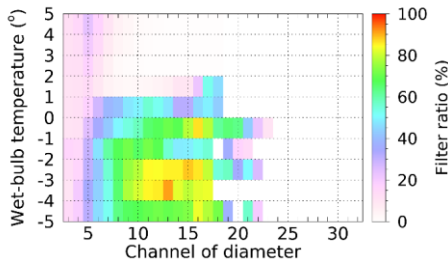
(b) Method 1 (melted)



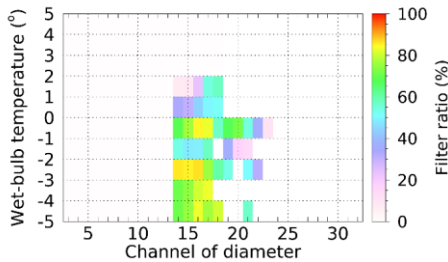
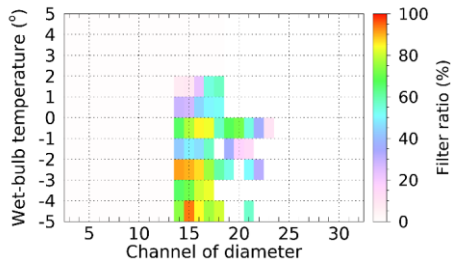
(d) Method 2 (melted)



(e) Method 3



(f) Method 3 (melted)



382 **Figure 13: Particle filter ratio by diameter channel for T_w according to the pre-processing method based on falling velocity.**

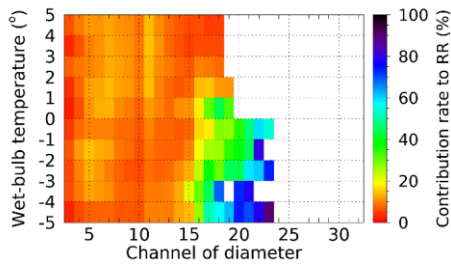
383 **4.5 Contribution rate by particle diameter to precipitation intensity**

384 Figure 14 shows the contribution rate of the number concentration by diameter to the precipitation intensity as derived from
 385 the disdrometer data. It is observed that when the T_w exceeds 1 °C, the contribution rate remains approximately 20% or lower
 386 across all diameters. Conversely, when T_w is below 1 °C, the concentration of particles measuring 3 mm (CH 15) or larger
 387 considerably influences the calculation of precipitation intensity. The contribution rate of 1.25 to 1.75 mm diameter (CH 11
 388 to 13) decreased when the temperature was lower than 1 °C. The decrease in the contribution rate of drops smaller than 3
 389 mm and the increase in the contribution rate of larger drops was as a result of the decrease in the concentration of drops
 390 smaller than 3 mm through the QC process (Section 4.4), which increased the impact of relatively larger drops on the
 391 calculation of precipitation intensity. This phenomenon can be attributed to the direct proportionality of the precipitation
 392 intensity to $N(D)$ and D^3 , indicating that an increase in the particle diameter substantially affected the results. After QC, a
 393 substantial increase in the contribution rate for a specific diameter may affect the precipitation intensity owing to a decrease
 394 in the concentration of drops in the diameter range with a lower contribution rate.

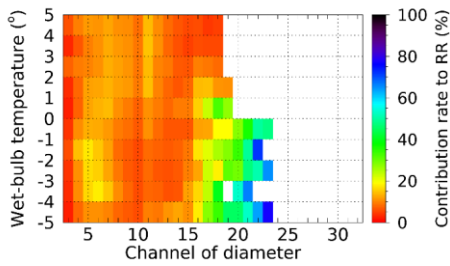
395 In scenarios where it is assumed that snow particles have melted, the diameter of these particles decreases, increasing the
 396 concentration of smaller particles. As a result, the contribution rate of diameter from approximately 0.5 to 1 mm (CH 5 to 10)

397 increased. Notably, in Method 3, there was a minimal removal of particles smaller than 2 mm, which resulted in negligible
 398 differences between the scenarios that accounted for the melted state of snow particles and those that did not.

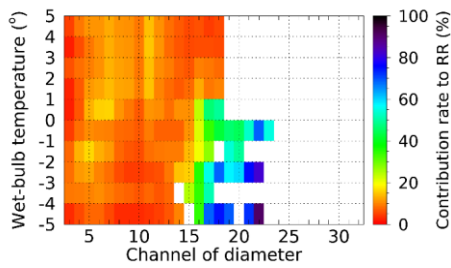
(a) Method 1



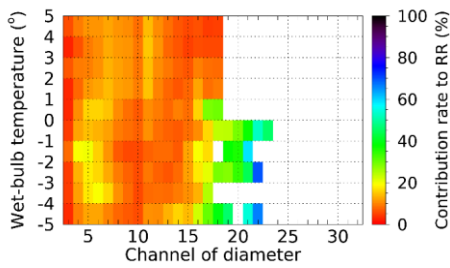
(b) Method 1 (melted)



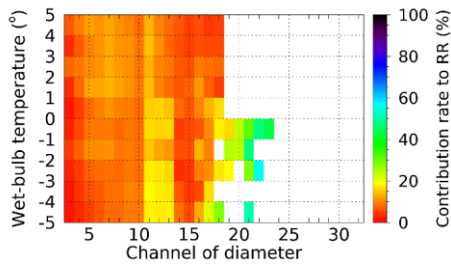
(c) Method 2



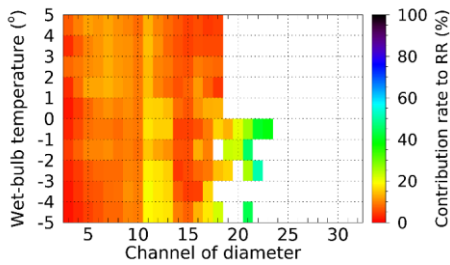
(d) Method 2 (melted)



(e) Method 3



(f) Method 3 (melted)



399 **Figure 14: Precipitation contribution rate by diameter channel for T_w using the pre-processing method based on falling velocity.**

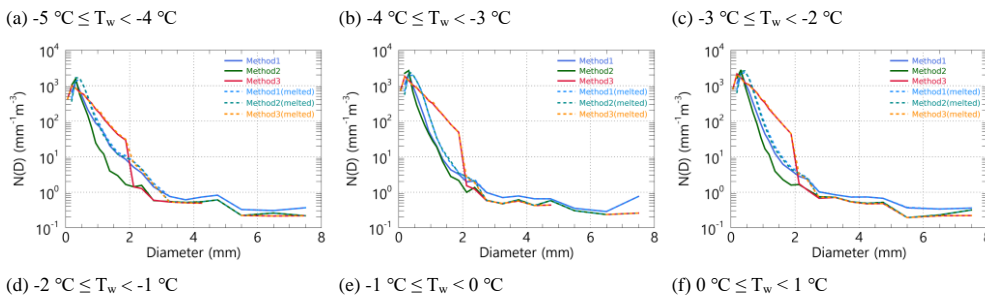
400 4.6 Drop size distribution

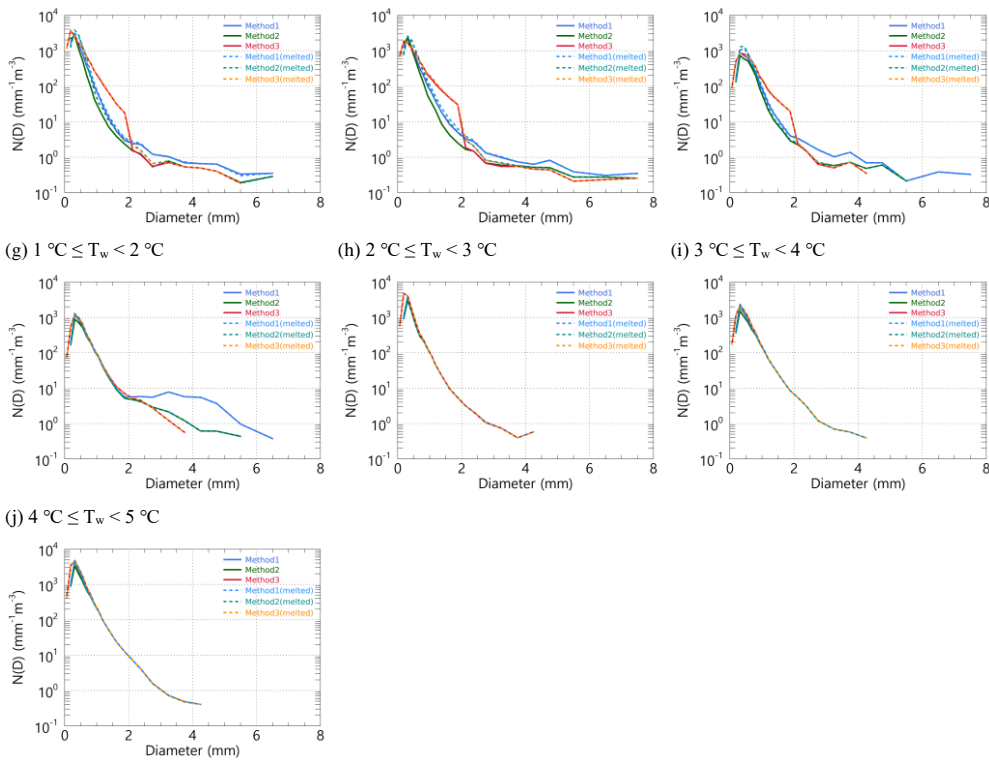
401 4.6.1 Number concentration calculated by applying QC methods based on T_w

402 The precipitation intensity derived from disdrometer data is contingent on the number concentration; therefore, examining
403 the distribution of the number concentration is imperative. Figure 15 shows the average distribution of the number
404 concentration obtained by applying the QC method under varying T_w conditions. Notably, when the temperature exceeded
405 2 °C, the distributions yielded by all QC methods were comparable. Method 3 exhibited a relatively high concentration of
406 small droplets measuring 1 mm or less, whereas the number of droplets measuring 1 mm or more showed minimal variation
407 (Fig. 15h). This finding indicates that, at temperatures above 2 °C, the output values remain consistent across different QC
408 methods.

409 At temperatures ranging from 1 to 2 °C, the distribution of particles exceeding 2 mm in size was distinctly differentiated
410 according to the QC method employed. This finding suggests that the fall velocity of particles larger than 2 mm exhibits
411 considerable variation within this temperature interval (Fig. 10). Conversely, at temperatures below 1 °C, the distribution
412 obtained through Method 3 displayed an anomalous pattern. This irregularity can be attributed to the failure of Method 3 to
413 exclude snow particles smaller than 2 mm, leading to a higher concentration than that of the other QC methods. When
414 considering the scenario in which particles are assumed to have melted, an increase in the concentration of water was
415 observed for particles with a diameter of 1 mm or less when the T_w was between 0 and 1 °C, while the concentration of
416 particles larger than 2 mm remained relatively unchanged.

417 In comparing scenarios where particles are assumed to have melted versus those that are not, no notable differences were
418 observed at temperatures exceeding 1 °C (see Fig. 15g). However, within the temperature range of 0 to 1°C, there was an
419 increase in the number of particles smaller than 1 mm. There was a similar distribution in the number of medium and larger
420 particles (1 mm or more). As the T_w progressively decreased below 0 °C, the disparity in the number concentration of
421 particles larger than 1 mm became more pronounced (Fig. 15(a-e)).





422 **Figure 15: Average number concentration distribution for T_w using pre-processing methods.**

423 **4.6.2 Difference in the number concentration based on the gamma model**

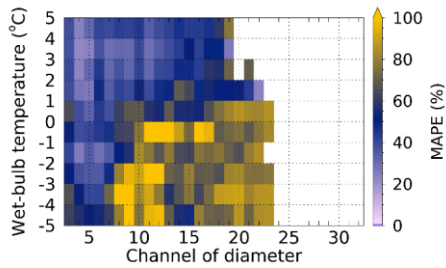
424 The change in the shape of the number concentration within the observed data has implications for DSD model parameters.
 425 The notable discrepancy between the observed number concentration and that derived from the model parameters raises
 426 concerns regarding the reliability of the DSD model.

427 Figures 16 and 17 show the variance between the observed number concentration and that predicted using the gamma model.
 428 When all QC methods were implemented, the MAPE remained below 60% across all diameter ranges at temperatures
 429 exceeding 2 °C. However, as the T_w fell below 1 °C, the discrepancy for diameters greater than 0.6 mm (CH 7) escalated to
 430 over 70%. At 2 °C or higher temperatures, the gamma distribution overestimated the concentration of particles smaller than 1

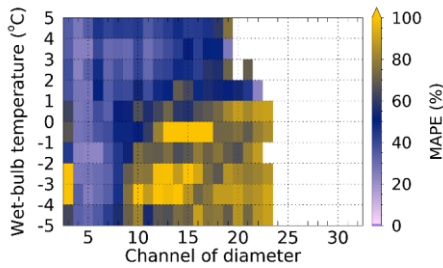
431 mm while underestimating those larger than 1 mm. Nonetheless, the extent of under- or over-simulation by gamma
432 distribution remained below 50% across all diameter intervals.

433 When T_w was below 1 °C, assuming that the snow particles had melted, the error rate in simulating the concentration of
434 particles smaller than 1 mm (CH 8) diminished (Fig. 16(b, d)). Concurrently, the percentage bias (PBAIS) for particle
435 diameters less than 1 mm decreased, approaching a value near zero (Fig. 17(b, d)). This phenomenon can be attributed to the
436 application of the QC method under subzero conditions, which led to an overestimation of the gamma distribution for
437 diameters of 1 mm or less because of the increased influence of smaller particles resulting from the exclusion of larger
438 particles exceeding 3 mm. Conversely, this resulted in an underestimation of the gamma distribution for diameters larger
439 than 3 mm.

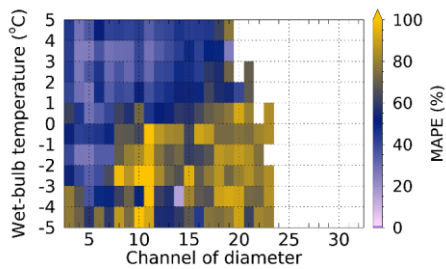
(a) Method 1



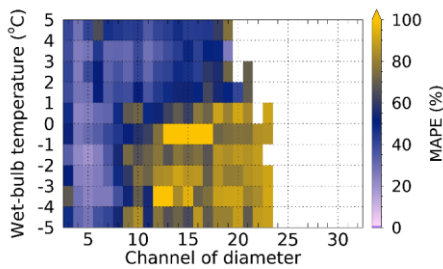
(b) Method 1 (melted)



(c) Method 2

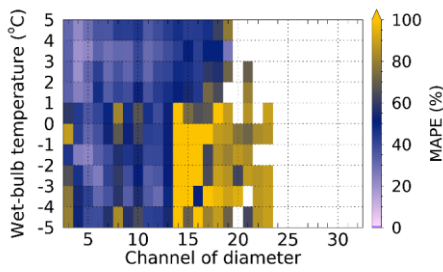
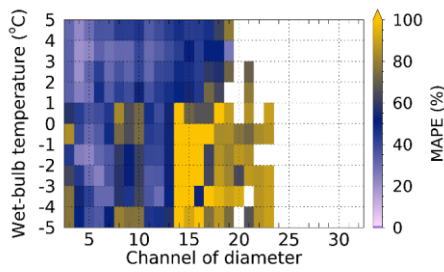


(d) Method 2 (melted)



(e) Method 3

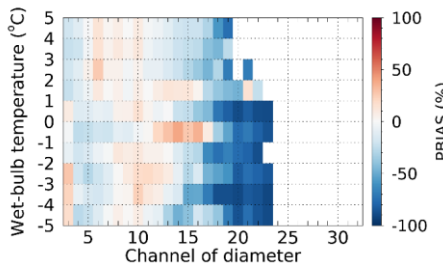
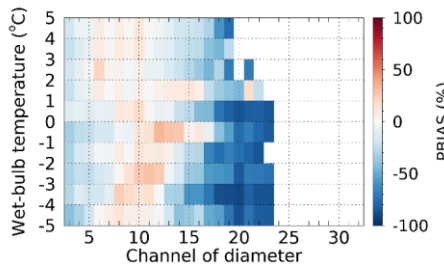
(f) Method 3 (melted)



440 **Figure 16: MAPE for diameter and wet-bulb temperature using the pre-processing method**

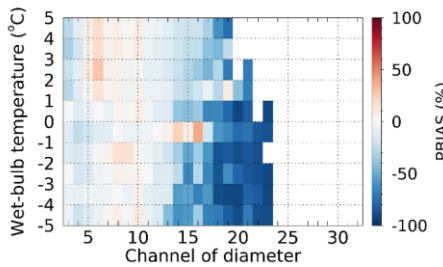
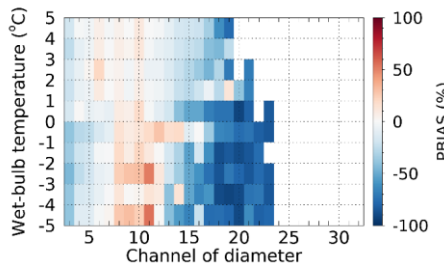
(a) Method 1

(b) Method 1 (melted)



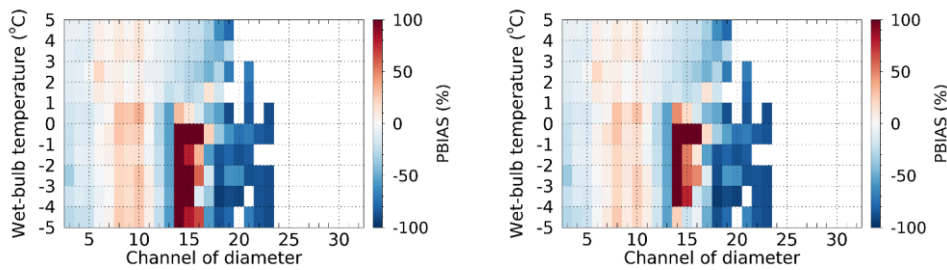
(c) Method 2

(d) Method 2 (melted)



(e) Method 3

(f) Method 3 (melted)



441 **Figure 17: PBAIS for diameter and wet-bulb temperature using the pre-processing method**

442 **5 Conclusion**

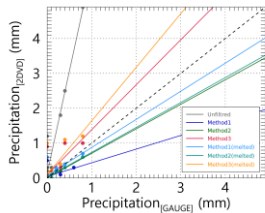
443 This study employed data collected from a 2DVD disdrometer in conjunction with traditional rain gauges to assess the
 444 precipitation measurements derived from the disdrometer under T_w conditions and to evaluate the reliability of the DSD
 445 model. Precipitation estimates derived from the quality control (QC) techniques implemented in this study exhibited a
 446 correlation coefficient of 0.98 or higher and an error rate of approximately 8.5% compared to precipitation measured by rain
 447 gauges under conditions where T_w was above 5 °C. Additionally, the QC-processed precipitation data mitigated the
 448 overestimation present when QC methods were not applied to the disdrometer data. These findings indicate that QC methods
 449 demonstrated high reliability under rainfall conditions.
 450 When both T_{air} and T_w were below 1 °C, the fall velocity of precipitation particles decreased significantly, with most
 451 velocities ranging from 0.5 to 3 m s⁻¹. This reduction results from a higher proportion of snow particles, which have a lower
 452 density than raindrops. These results are consistent with Ding et al. (2014), who reported that the proportion of raindrops
 453 decreases to less than 30% at temperatures below this threshold. When T_{air} ranged from 1 to 3 °C, the distribution of fall
 454 velocities was broader compared to cases where T_w was within the same interval, and deviations from the terminal velocity
 455 of raindrops were more pronounced. Therefore, hydrometeor classification during the QC process of disdrometer data should
 456 employ T_w as the primary environmental parameter for fall velocity analysis. This approach reduces errors in particle
 457 removal related to fall velocity distribution and improves the reliability of long-term rainfall measurements. As T_w decreased
 458 below 2 °C, quantitative precipitation errors increased because the filter ratio for particles of 3 mm or less rose to 30% or
 459 higher. In this temperature range, the likely coexistence of raindrops and solid particles reduces the reliability of
 460 conventional rainfall quality control methods. When snow particles are assumed to have melted, the correlation coefficient
 461 approached 0.9 even within the 0 to 1 °C range, and error variability decreased. These findings indicate that precipitation
 462 calculation reliability can be maintained under mixed-phase conditions (0 to 2 °C) if an appropriate snow particle density is
 463 applied. Verification of precipitation using a weighing rain gauge is recommended when T_w falls below 2 °C.

464 For DSD characteristics, the DSD shape remained consistent across different quality control methods at T_w above 2 °C.
 465 Below 2 °C, Method 1 (+40% terminal velocity criterion) resulted in a higher number concentration of drops larger than 2
 466 mm. In contrast, below 1 °C, Method 3 (Raupach et al., 2015) produced a pronounced, irregular distribution of number
 467 concentrations for diameters of 1 to 2 mm. These distortions in DSD shape, which depend on the quality control method,
 468 raise concerns regarding the reliability of derived DSD parameters. Consequently, only disdrometer data collected at T_w
 469 above 2 °C should be used to calculate DSD parameters and DSD-based rain rates.
 470 Ensuring the reliability of dual-polarimetric radar-based quantitative precipitation estimation (QPE) parameterized by DSD
 471 characteristics is essential, given that DSD characteristics derived from disdrometer data vary with temperature. These
 472 temperature-dependent variations in DSD directly influence dual-polarimetric parameters and are likely to affect the QPE
 473 relationships used in radar-based precipitation estimation. Therefore, further research is required to investigate the impact of
 474 disdrometer data quality on QPE accuracy under different temperature conditions. This study employed data collected from a
 475 2DVD disdrometer in conjunction with traditional rain gauges to assess the precipitation measurements derived from the
 476 disdrometer under T_w conditions and to evaluate the reliability of the DSD model.

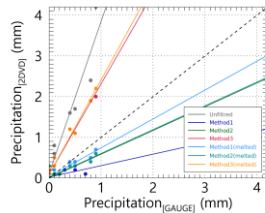
477 Appendices

478 Figures A1 and A2 present the findings from a comparative analysis of hourly accumulated precipitation intensity, derived
 479 from observations using the 2DVD and two types of rain gauges (A1~A6 represents the tipping-bucket type and A7~A12
 480 represents the weighing type) under the specified T_w interval conditions at 1 °C intervals. In each figure, the solid line
 481 denotes the regression line correlating the precipitation intensities derived by applying each quality control (QC) method.
 482 The constants and validation indices associated with the regression lines are listed in Tables A1 and A2, respectively.
 483 Tables A3 and A4 provide details regarding the diameter and velocity channels used to calculate the number concentration
 484 based on 2DVD data. The channel information corresponded to the values employed in the PARSIVEL disdrometer data.

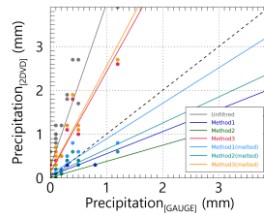
(a) $-5\text{ °C} \leq T_w < -4\text{ °C}$



(b) $-4\text{ °C} \leq T_w < -3\text{ °C}$



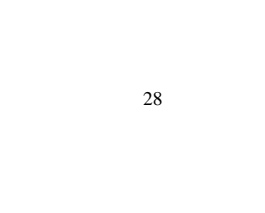
(c) $-3\text{ °C} \leq T_w < -2\text{ °C}$



(d) $-2\text{ °C} \leq T_w < -1\text{ °C}$

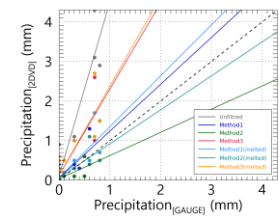


(e) $-1\text{ °C} \leq T_w < 0\text{ °C}$

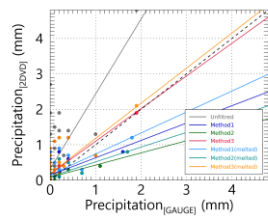


(f) $0\text{ °C} \leq T_w < 1\text{ °C}$

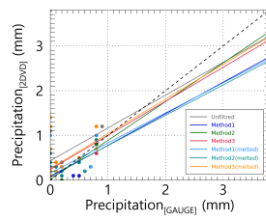




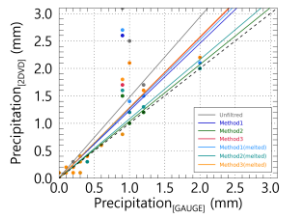
(g) $1\text{ }^{\circ}\text{C} \leq T_w < 2\text{ }^{\circ}\text{C}$



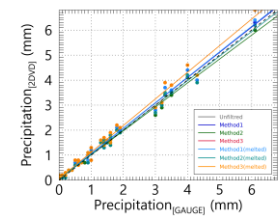
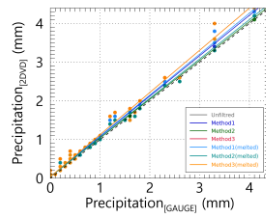
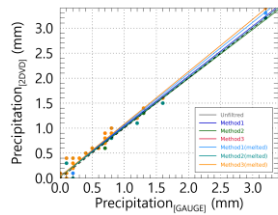
(h) $2\text{ }^{\circ}\text{C} \leq T_w < 3\text{ }^{\circ}\text{C}$



(i) $3\text{ }^{\circ}\text{C} \leq T_w < 4\text{ }^{\circ}\text{C}$



(j) $4\text{ }^{\circ}\text{C} \leq T_w < 5\text{ }^{\circ}\text{C}$

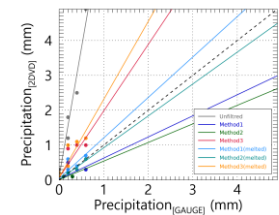


485 **Figure A1: Precipitation intensity scatter plot based on tipping-bucket rain gauge and 2DVD observation data for each T_w range.**
 486 **Each color in the scatter plot represents a filtering method.**

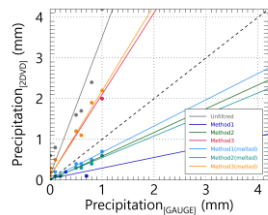
(a) $-5\text{ }^{\circ}\text{C} \leq T_w < -4\text{ }^{\circ}\text{C}$

(b) $-4\text{ }^{\circ}\text{C} \leq T_w < -3\text{ }^{\circ}\text{C}$

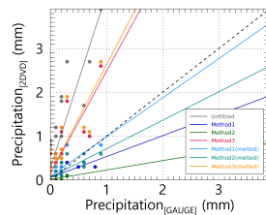
(c) $-3\text{ }^{\circ}\text{C} \leq T_w < -2\text{ }^{\circ}\text{C}$



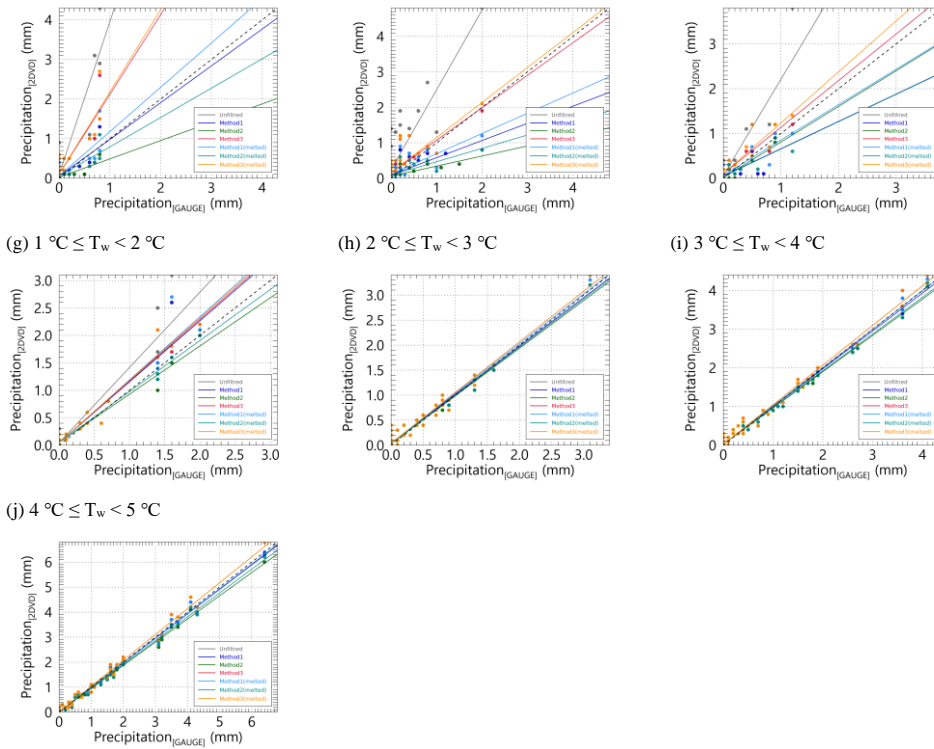
(d) $-2\text{ }^{\circ}\text{C} \leq T_w < -1\text{ }^{\circ}\text{C}$



(e) $-1\text{ }^{\circ}\text{C} \leq T_w < 0\text{ }^{\circ}\text{C}$



(f) $0\text{ }^{\circ}\text{C} \leq T_w < 1\text{ }^{\circ}\text{C}$



487 **Figure A2:** Precipitation intensity scatter plot based on weighing rain gauge and 2DVD observation data for each T_w range. Each
 488 color in the scatter plot represents a filtering method.

489 **Table A1:** a_i of precipitation intensity derived from tipping-bucket rain gauge and 2DVD observations for each T_w range.

a_i	T1	T2	T3	T4	T5	T6	T7	T8	T9	T10
Unfiltered	5.88	3.74	3.72	4.40	2.11	0.73	1.46	1.05	1.09	1.06
Method 1	0.39	0.28	0.51	1.18	0.49	0.71	1.23	1.00	1.04	1.01
Method 2	0.70	0.58	0.37	0.59	0.34	0.87	1.03	0.98	1.00	0.96
Method 3	1.29	2.22	2.30	2.18	0.92	0.76	1.28	1.05	1.09	1.06
Method 1 (melted)	0.81	0.71	0.81	1.29	0.59	0.67	1.26	1.03	1.06	1.02

<u>Method 2</u> (melted)	<u>0.71</u>	<u>0.59</u>	<u>0.60</u>	<u>0.86</u>	<u>0.42</u>	<u>0.68</u>	<u>1.08</u>	<u>0.99</u>	<u>1.02</u>	<u>0.98</u>
<u>Method 3</u> (melted)	<u>1.54</u>	<u>2.33</u>	<u>2.41</u>	<u>2.25</u>	<u>0.99</u>	<u>0.77</u>	<u>1.29</u>	<u>1.05</u>	<u>1.09</u>	<u>1.06</u>

490 **Table A2: a_0 of precipitation intensity derived from tipping-bucket rain gauge and 2DVD observations for each T_w range.**

a_0	T1	T2	T3	T4	T5	T6	T7	T8	T9	T10
<u>Unfiltered</u>	<u>0.12</u>	<u>0.11</u>	<u>0.25</u>	<u>0.11</u>	<u>0.32</u>	<u>0.43</u>	<u>0.01</u>	<u>0.04</u>	<u>0.04</u>	<u>0.06</u>
<u>Method 1</u>	<u>0.04</u>	<u>0.02</u>	<u>0.05</u>	<u>0.06</u>	<u>0.14</u>	<u>0.07</u>	<u>0.01</u>	<u>0.04</u>	<u>0.04</u>	<u>0.05</u>
<u>Method 2</u>	<u>0.01</u>	<u>0.00</u>	<u>0.01</u>	<u>0.03</u>	<u>0.08</u>	<u>0.02</u>	<u>0.00</u>	<u>0.03</u>	<u>0.04</u>	<u>0.06</u>
<u>Method 3</u>	<u>0.09</u>	<u>0.09</u>	<u>0.12</u>	<u>0.13</u>	<u>0.18</u>	<u>0.24</u>	<u>0.00</u>	<u>0.04</u>	<u>0.04</u>	<u>0.06</u>
<u>Method 1</u> (melted)	<u>0.07</u>	<u>0.03</u>	<u>0.08</u>	<u>0.07</u>	<u>0.15</u>	<u>0.16</u>	<u>0.01</u>	<u>0.04</u>	<u>0.03</u>	<u>0.05</u>
<u>Method 2</u> (melted)	<u>0.02</u>	<u>0.02</u>	<u>0.06</u>	<u>0.06</u>	<u>0.10</u>	<u>0.10</u>	<u>0.00</u>	<u>0.03</u>	<u>0.04</u>	<u>0.05</u>
<u>Method 3</u> (melted)	<u>0.10</u>	<u>0.08</u>	<u>0.14</u>	<u>0.13</u>	<u>0.19</u>	<u>0.26</u>	<u>0.00</u>	<u>0.04</u>	<u>0.04</u>	<u>0.06</u>

491 **Table A3: RMSE of precipitation intensity derived from tipping-bucket rain gauge and 2DVD observations for each T_w range.**

RMSE	T1	T2	T3	T4	T5	T6	T7	T8	T9	T10
<u>Unfiltered</u>	<u>1.01</u>	<u>0.91</u>	<u>0.92</u>	<u>0.96</u>	<u>0.85</u>	<u>0.92</u>	<u>0.46</u>	<u>0.10</u>	<u>0.17</u>	<u>0.23</u>
<u>Method 1</u>	<u>0.17</u>	<u>0.18</u>	<u>0.12</u>	<u>0.21</u>	<u>0.29</u>	<u>0.20</u>	<u>0.30</u>	<u>0.09</u>	<u>0.12</u>	<u>0.16</u>
<u>Method 2</u>	<u>0.03</u>	<u>0.03</u>	<u>0.06</u>	<u>0.13</u>	<u>0.20</u>	<u>0.09</u>	<u>0.12</u>	<u>0.08</u>	<u>0.08</u>	<u>0.13</u>
<u>Method 3</u>	<u>0.24</u>	<u>0.44</u>	<u>0.47</u>	<u>0.49</u>	<u>0.33</u>	<u>0.43</u>	<u>0.25</u>	<u>0.10</u>	<u>0.17</u>	<u>0.23</u>
<u>Method 1</u> (melted)	<u>0.16</u>	<u>0.10</u>	<u>0.15</u>	<u>0.25</u>	<u>0.28</u>	<u>0.31</u>	<u>0.32</u>	<u>0.09</u>	<u>0.13</u>	<u>0.16</u>
<u>Method 2</u> (melted)	<u>0.09</u>	<u>0.14</u>	<u>0.15</u>	<u>0.17</u>	<u>0.25</u>	<u>0.21</u>	<u>0.14</u>	<u>0.08</u>	<u>0.09</u>	<u>0.13</u>
<u>Method 3</u> (melted)	<u>0.27</u>	<u>0.46</u>	<u>0.51</u>	<u>0.51</u>	<u>0.35</u>	<u>0.46</u>	<u>0.26</u>	<u>0.10</u>	<u>0.17</u>	<u>0.23</u>

492 **Table A4: MAE of precipitation intensity derived from tipping-bucket rain gauge and 2DVD observations for each T_w range.**

MAE	T1	T2	T3	T4	T5	T6	T7	T8	T9	T10
<u>Unfiltered</u>	<u>0.44</u>	<u>0.47</u>	<u>0.56</u>	<u>0.45</u>	<u>0.45</u>	<u>0.40</u>	<u>0.16</u>	<u>0.06</u>	<u>0.10</u>	<u>0.16</u>
<u>Method 1</u>	<u>0.08</u>	<u>0.07</u>	<u>0.05</u>	<u>0.11</u>	<u>0.15</u>	<u>0.11</u>	<u>0.10</u>	<u>0.06</u>	<u>0.07</u>	<u>0.12</u>

<u>Method 2</u>	<u>0.01</u>	<u>0.01</u>	<u>0.04</u>	<u>0.07</u>	<u>0.10</u>	<u>0.06</u>	<u>0.05</u>	<u>0.05</u>	<u>0.05</u>	<u>0.09</u>
<u>Method 3</u>	<u>0.11</u>	<u>0.26</u>	<u>0.28</u>	<u>0.26</u>	<u>0.18</u>	<u>0.23</u>	<u>0.10</u>	<u>0.06</u>	<u>0.10</u>	<u>0.16</u>
<u>Method 1 (melted)</u>	<u>0.06</u>	<u>0.05</u>	<u>0.09</u>	<u>0.12</u>	<u>0.16</u>	<u>0.16</u>	<u>0.11</u>	<u>0.06</u>	<u>0.08</u>	<u>0.12</u>
<u>Method 2 (melted)</u>	<u>0.05</u>	<u>0.07</u>	<u>0.08</u>	<u>0.09</u>	<u>0.13</u>	<u>0.12</u>	<u>0.06</u>	<u>0.05</u>	<u>0.05</u>	<u>0.10</u>
<u>Method 3 (melted)</u>	<u>0.13</u>	<u>0.27</u>	<u>0.30</u>	<u>0.28</u>	<u>0.20</u>	<u>0.25</u>	<u>0.11</u>	<u>0.06</u>	<u>0.10</u>	<u>0.16</u>

493 **Table A5: MAPE of precipitation intensity derived from tipping-bucket rain gauge and 2DVD observations for each T_w range.**

<u>MAPE</u>	<u>T1</u>	<u>T2</u>	<u>T3</u>	<u>T4</u>	<u>T5</u>	<u>T6</u>	<u>T7</u>	<u>T8</u>	<u>T9</u>	<u>T10</u>
<u>Unfiltered</u>	<u>48.71</u>	<u>55.32</u>	<u>60.15</u>	<u>50.58</u>	<u>50.86</u>	<u>43.25</u>	<u>34.45</u>	<u>15.68</u>	<u>13.54</u>	<u>21.14</u>
<u>Method 1</u>	<u>28.57</u>	<u>56.67</u>	<u>27.24</u>	<u>34.01</u>	<u>37.07</u>	<u>56.39</u>	<u>31.27</u>	<u>17.96</u>	<u>12.04</u>	<u>16.83</u>
<u>Method 2</u>	<u>5.56</u>	<u>11.11</u>	<u>23.81</u>	<u>57.78</u>	<u>41.67</u>	<u>26.56</u>	<u>26.79</u>	<u>12.78</u>	<u>10.54</u>	<u>13.44</u>
<u>Method 3</u>	<u>38.75</u>	<u>49.04</u>	<u>51.11</u>	<u>47.07</u>	<u>45.58</u>	<u>46.25</u>	<u>25.58</u>	<u>15.68</u>	<u>13.54</u>	<u>21.14</u>
<u>Method 1 (melted)</u>	<u>26.33</u>	<u>21.39</u>	<u>34.06</u>	<u>31.87</u>	<u>42.73</u>	<u>38.50</u>	<u>31.64</u>	<u>18.03</u>	<u>12.37</u>	<u>16.51</u>
<u>Method 2 (melted)</u>	<u>17.78</u>	<u>23.33</u>	<u>27.88</u>	<u>31.87</u>	<u>45.37</u>	<u>44.88</u>	<u>27.62</u>	<u>12.84</u>	<u>11.00</u>	<u>15.80</u>
<u>Method 3 (melted)</u>	<u>40.50</u>	<u>49.24</u>	<u>50.27</u>	<u>47.38</u>	<u>46.46</u>	<u>45.30</u>	<u>28.44</u>	<u>15.68</u>	<u>13.54</u>	<u>21.14</u>

494 **Table A6: CC of precipitation intensity derived from tipping-bucket rain gauge and 2DVD observations for each T_w range.**

<u>CC</u>	<u>T1</u>	<u>T2</u>	<u>T3</u>	<u>T4</u>	<u>T5</u>	<u>T6</u>	<u>T7</u>	<u>T8</u>	<u>T9</u>	<u>T10</u>
<u>Unfiltered</u>	<u>0.97</u>	<u>0.97</u>	<u>0.93</u>	<u>0.95</u>	<u>0.74</u>	<u>0.23</u>	<u>0.85</u>	<u>0.99</u>	<u>0.99</u>	<u>0.99</u>
<u>Method 1</u>	<u>0.45</u>	<u>0.75</u>	<u>0.78</u>	<u>0.79</u>	<u>0.55</u>	<u>0.66</u>	<u>0.89</u>	<u>0.99</u>	<u>1.00</u>	<u>0.99</u>
<u>Method 2</u>	<u>0.98</u>	<u>0.94</u>	<u>0.60</u>	<u>0.67</u>	<u>0.57</u>	<u>0.91</u>	<u>0.97</u>	<u>0.99</u>	<u>1.00</u>	<u>1.00</u>
<u>Method 3</u>	<u>0.76</u>	<u>0.99</u>	<u>0.94</u>	<u>0.87</u>	<u>0.73</u>	<u>0.47</u>	<u>0.94</u>	<u>0.99</u>	<u>0.99</u>	<u>0.99</u>
<u>Method 1 (melted)</u>	<u>0.76</u>	<u>0.97</u>	<u>0.85</u>	<u>0.82</u>	<u>0.66</u>	<u>0.51</u>	<u>0.88</u>	<u>0.99</u>	<u>1.00</u>	<u>0.99</u>
<u>Method 2 (melted)</u>	<u>0.93</u>	<u>0.98</u>	<u>0.84</u>	<u>0.79</u>	<u>0.67</u>	<u>0.65</u>	<u>0.96</u>	<u>0.99</u>	<u>1.00</u>	<u>1.00</u>
<u>Method 3 (melted)</u>	<u>0.79</u>	<u>0.99</u>	<u>0.93</u>	<u>0.87</u>	<u>0.74</u>	<u>0.45</u>	<u>0.93</u>	<u>0.99</u>	<u>0.99</u>	<u>0.99</u>

495 **Table A7: a_1 of precipitation intensity derived from weighing rain gauge and 2DVD observations for each T_w range.**

a_l	T1	T2	T3	T4	T5	T6	T7	T8	T9	T10
Unfiltered	7.36	3.39	3.98	3.86	2.25	2.15	1.37	1.01	1.03	1.03
Method 1	0.61	0.26	0.48	0.93	0.48	0.61	1.11	0.97	0.98	0.98
Method 2	0.53	0.58	0.21	0.46	0.28	0.80	0.88	0.95	0.94	0.93
Method 3	1.91	2.01	2.33	2.02	0.92	1.04	1.12	1.01	1.03	1.03
Method 1 (melted)	1.16	0.65	0.89	1.12	0.57	0.79	1.15	0.99	0.99	0.98
Method 2 (melted)	0.91	0.53	0.65	0.74	0.38	0.61	0.93	0.96	0.95	0.95
Method 3 (melted)	2.24	2.10	2.47	2.08	0.99	1.14	1.13	1.01	1.03	1.03

496 **Table A8: a_0 of precipitation intensity derived from weighing rain gauge and 2DVD observations for each T_w range.**

a_0	T1	T2	T3	T4	T5	T6	T7	T8	T9	T10
Unfiltered	0.09	0.12	0.27	0.09	0.24	0.06	0.04	0.04	0.02	0.01
Method 1	0.02	0.03	0.06	0.05	0.09	0.05	0.04	0.05	0.02	0.01
Method 2	0.01	0.00	0.01	0.03	0.06	0.01	0.05	0.03	0.03	0.02
Method 3	0.07	0.10	0.15	0.10	0.15	0.10	0.05	0.04	0.02	0.01
Method 1 (melted)	0.05	0.03	0.09	0.06	0.12	0.06	0.04	0.04	0.02	0.01
Method 2 (melted)	0.01	0.02	0.07	0.05	0.09	0.04	0.05	0.04	0.02	0.01
Method 3 (melted)	0.07	0.10	0.16	0.11	0.16	0.10	0.05	0.04	0.02	0.01

497 **Table A9: RMSE of precipitation intensity derived from weighing rain gauge and 2DVD observations for each T_w range.**

RMSE	T1	T2	T3	T4	T5	T6	T7	T8	T9	T10
Unfiltered	1.04	0.88	0.95	0.93	0.76	0.64	0.33	0.14	0.12	0.17
Method 1	0.13	0.17	0.13	0.19	0.28	0.20	0.20	0.13	0.10	0.14

Method 2	0.07	0.03	0.09	0.18	0.31	0.10	0.11	0.12	0.11	0.17
Method 3	0.22	0.41	0.52	0.45	0.29	0.21	0.16	0.14	0.12	0.17
Method 1 (melted)	0.11	0.13	0.16	0.23	0.26	0.16	0.21	0.13	0.10	0.13
Method 2 (melted)	0.04	0.18	0.14	0.17	0.29	0.18	0.09	0.12	0.11	0.15
Method 3 (melted)	0.27	0.44	0.55	0.48	0.30	0.22	0.16	0.14	0.12	0.17

498 **Table A10: MAE of precipitation intensity derived from weighing rain gauge and 2DVD observations for each T_w range.**

MAE	T1	T2	T3	T4	T5	T6	T7	T8	T9	T10
Unfiltered	0.44	0.46	0.57	0.43	0.43	0.31	0.15	0.08	0.07	0.12
Method 1	0.06	0.07	0.07	0.12	0.13	0.11	0.10	0.08	0.07	0.10
Method 2	0.02	0.01	0.06	0.11	0.15	0.07	0.07	0.07	0.07	0.12
Method 3	0.12	0.25	0.29	0.24	0.16	0.13	0.09	0.08	0.07	0.12
Method 1 (melted)	0.06	0.08	0.10	0.11	0.15	0.10	0.09	0.08	0.06	0.10
Method 2 (melted)	0.01	0.10	0.09	0.11	0.14	0.10	0.06	0.07	0.07	0.11
Method 3 (melted)	0.14	0.26	0.32	0.25	0.17	0.14	0.09	0.08	0.07	0.12

499 **Table A11: MAPE of precipitation intensity derived from weighing rain gauge and 2DVD observations for each T_w range.**

MAPE	T1	T2	T3	T4	T5	T6	T7	T8	T9	T10
Unfiltered	49.76	55.42	60.80	48.81	53.44	41.61	41.39	22.03	13.07	19.05
Method 1	25.71	63.33	41.35	41.49	36.12	79.17	38.21	22.17	14.21	21.89
Method 2	22.22	11.11	28.57	85.56	55.43	27.34	35.56	18.32	14.12	20.69
Method 3	42.13	49.58	52.32	44.83	46.50	37.92	34.21	22.03	13.07	19.05

<u>Method 1</u> <u>(melted)</u>	<u>30.25</u>	<u>31.05</u>	<u>36.50</u>	<u>29.44</u>	<u>49.92</u>	<u>32.10</u>	<u>37.80</u>	<u>22.22</u>	<u>13.91</u>	<u>21.50</u>
<u>Method 2</u> <u>(melted)</u>	<u>8.89</u>	<u>35.56</u>	<u>34.62</u>	<u>42.75</u>	<u>58.79</u>	<u>40.35</u>	<u>34.42</u>	<u>17.78</u>	<u>14.24</u>	<u>22.16</u>
<u>Method 3</u> <u>(melted)</u>	<u>43.48</u>	<u>49.81</u>	<u>51.47</u>	<u>45.14</u>	<u>46.83</u>	<u>38.15</u>	<u>37.14</u>	<u>22.03</u>	<u>13.07</u>	<u>19.05</u>

500 **Table A12: CC of precipitation intensity derived from weighing rain gauge and 2DVD observations for each Tw range.**

<u>CC</u>	<u>T1</u>	<u>T2</u>	<u>T3</u>	<u>T4</u>	<u>T5</u>	<u>T6</u>	<u>T7</u>	<u>T8</u>	<u>T9</u>	<u>T10</u>
<u>Unfiltered</u>	<u>0.98</u>	<u>0.97</u>	<u>0.90</u>	<u>0.93</u>	<u>0.88</u>	<u>0.89</u>	<u>0.95</u>	<u>0.98</u>	<u>0.99</u>	<u>0.99</u>
<u>Method 1</u>	<u>0.70</u>	<u>0.65</u>	<u>0.73</u>	<u>0.80</u>	<u>0.79</u>	<u>0.71</u>	<u>0.96</u>	<u>0.98</u>	<u>0.99</u>	<u>1.00</u>
<u>Method 2</u>	<u>0.82</u>	<u>0.94</u>	<u>0.45</u>	<u>0.75</u>	<u>0.78</u>	<u>0.92</u>	<u>0.98</u>	<u>0.98</u>	<u>1.00</u>	<u>1.00</u>
<u>Method 3</u>	<u>0.91</u>	<u>0.98</u>	<u>0.86</u>	<u>0.90</u>	<u>0.80</u>	<u>0.90</u>	<u>0.98</u>	<u>0.98</u>	<u>0.99</u>	<u>0.99</u>
<u>Method 1</u> <u>(melted)</u>	<u>0.90</u>	<u>0.97</u>	<u>0.82</u>	<u>0.82</u>	<u>0.77</u>	<u>0.89</u>	<u>0.96</u>	<u>0.98</u>	<u>1.00</u>	<u>1.00</u>
<u>Method 2</u> <u>(melted)</u>	<u>0.98</u>	<u>0.98</u>	<u>0.79</u>	<u>0.82</u>	<u>0.77</u>	<u>0.87</u>	<u>0.99</u>	<u>0.98</u>	<u>1.00</u>	<u>1.00</u>
<u>Method 3</u> <u>(melted)</u>	<u>0.93</u>	<u>0.98</u>	<u>0.86</u>	<u>0.89</u>	<u>0.82</u>	<u>0.92</u>	<u>0.98</u>	<u>0.98</u>	<u>0.99</u>	<u>0.99</u>

501 **Table A13: Diameter channel information of the PARSIVEL disdrometer.**

<u>Channel number</u>	<u>Mid-value of channel (mm)</u>	<u>Diameter spread (mm)</u>	<u>Channel number</u>	<u>Mid-value of channel (mm)</u>	<u>Diameter spread (mm)</u>
<u>1</u>	<u>0.062</u>	<u>0.125</u>	<u>17</u>	<u>3.250</u>	<u>0.500</u>
<u>2</u>	<u>0.187</u>	<u>0.125</u>	<u>18</u>	<u>3.750</u>	<u>0.500</u>
<u>3</u>	<u>0.312</u>	<u>0.125</u>	<u>19</u>	<u>4.250</u>	<u>0.500</u>
<u>4</u>	<u>0.437</u>	<u>0.125</u>	<u>20</u>	<u>4.750</u>	<u>0.500</u>
<u>5</u>	<u>0.562</u>	<u>0.125</u>	<u>21</u>	<u>5.500</u>	<u>1.000</u>
<u>6</u>	<u>0.687</u>	<u>0.125</u>	<u>22</u>	<u>6.500</u>	<u>1.000</u>

7	0.812	0.125	23	7.500	1.000
8	0.937	0.125	24	8.500	1.000
9	1.062	0.125	25	9.500	1.000
10	1.187	0.125	26	11.000	2.000
11	1.375	0.250	27	13.000	2.000
12	1.625	0.250	28	15.000	2.000
13	1.875	0.250	29	17.000	2.000
14	2.125	0.250	30	19.000	2.000
15	2.375	0.250	31	21.500	3.000
16	2.750	0.500	32	24.500	3.000

502 **Table A14: Velocity channel information of the PARSIVEL disdrometer.**

Channel number	Mid-value of channel (mm)	Velocity spread (mm)	Channel number	Mid-value of channel (mm)	Velocity spread (mm)
1	0.050	0.100	17	2.600	0.400
2	0.150	0.100	18	3.000	0.400
3	0.250	0.100	19	3.400	0.400
4	0.350	0.100	20	3.800	0.400
5	0.450	0.100	21	4.400	0.800
6	0.550	0.100	22	5.200	0.800
7	0.650	0.100	23	6.000	0.800
8	0.750	0.100	24	6.800	0.800
9	0.850	0.100	25	7.600	0.800
10	0.950	0.100	26	8.800	1.600
11	1.100	0.200	27	10.400	1.600
12	1.300	0.200	28	12.000	1.600
13	1.500	0.200	29	13.600	1.600
14	1.700	0.200	30	15.200	1.600
15	1.900	0.200	31	17.600	3.200
16	2.200	0.400	32	20.800	3.200

503 **Table A1: Comparison of precipitation intensity based on tipping bucket rain gauge and 2DVD observation data for each T_n range.**

		T1	T2	T3	T4	T5	T6	T7	T8	T9	T10
Unfiltered	α	5.88	3.74	3.72	4.40	2.11	0.73	1.46	1.05	1.09	1.06

	α_u	0.12	0.11	0.25	0.11	0.32	0.43	0.01	0.04	0.04	0.06
	RMSE	1.01	0.91	0.92	0.96	0.85	0.92	0.46	0.10	0.17	0.23
	MAE	0.44	0.47	0.56	0.45	0.45	0.40	0.16	0.06	0.10	0.16
	MAPE	48.71	55.32	60.15	50.58	50.86	43.25	34.45	15.68	13.54	21.14
	CC	0.97	0.97	0.93	0.95	0.74	0.23	0.85	0.99	0.99	0.99
Method-1	α_r	0.39	0.28	0.51	1.18	0.49	0.71	1.23	1.00	1.04	1.01
	α_u	0.04	0.02	0.05	0.06	0.14	0.07	0.01	0.04	0.04	0.05
	RMSE	0.17	0.18	0.12	0.21	0.29	0.20	0.30	0.09	0.12	0.16
	MAE	0.08	0.07	0.05	0.11	0.15	0.11	0.10	0.06	0.07	0.12
	MAPE	28.57	56.67	27.24	34.01	37.07	56.39	31.27	17.96	12.04	16.83
CC	0.45	0.75	0.78	0.79	0.55	0.66	0.89	0.99	1.00	0.99	
Method-2	α_r	0.70	0.58	0.37	0.59	0.34	0.87	1.03	0.98	1.00	0.96
	α_u	0.01	0.00	0.01	0.03	0.08	0.02	0.00	0.03	0.04	0.06
	RMSE	0.03	0.03	0.06	0.13	0.20	0.09	0.12	0.08	0.08	0.13
	MAE	0.01	0.01	0.04	0.07	0.10	0.06	0.05	0.05	0.05	0.09
	MAPE	5.56	11.11	23.81	57.78	41.67	26.56	26.79	12.78	10.54	13.44
CC	0.98	0.94	0.60	0.67	0.57	0.91	0.97	0.99	1.00	1.00	
Method-3	α_r	1.29	2.22	2.30	2.18	0.92	0.76	1.28	1.05	1.09	1.06
	α_u	0.09	0.09	0.12	0.13	0.18	0.24	0.00	0.04	0.04	0.06
	RMSE	0.24	0.44	0.47	0.49	0.33	0.43	0.25	0.10	0.17	0.23
	MAE	0.11	0.26	0.28	0.26	0.18	0.23	0.10	0.06	0.10	0.16
	MAPE	38.75	49.04	51.11	47.07	45.58	46.25	25.58	15.68	13.54	21.14
CC	0.76	0.99	0.94	0.87	0.73	0.47	0.94	0.99	0.99	0.99	
Method-1 (melted)	α_r	0.81	0.71	0.81	1.29	0.59	0.67	1.26	1.03	1.06	1.02
	α_u	0.07	0.03	0.08	0.07	0.15	0.16	0.01	0.04	0.03	0.05
	RMSE	0.16	0.10	0.15	0.25	0.28	0.31	0.32	0.09	0.13	0.16
	MAE	0.06	0.05	0.09	0.12	0.16	0.16	0.11	0.06	0.08	0.12
	MAPE	26.33	21.39	34.06	31.87	42.73	38.50	31.64	18.03	12.37	16.51
CC	0.76	0.97	0.85	0.82	0.66	0.51	0.88	0.99	1.00	0.99	
Method-2 (melted)	α_r	0.71	0.59	0.60	0.86	0.42	0.68	1.08	0.99	1.02	0.98
	α_u	0.02	0.02	0.06	0.06	0.10	0.10	0.00	0.03	0.04	0.05
	RMSE	0.09	0.14	0.15	0.17	0.25	0.21	0.14	0.08	0.09	0.13
	MAE	0.05	0.07	0.08	0.09	0.13	0.12	0.06	0.05	0.05	0.10
	MAPE	17.78	23.33	27.88	31.87	45.37	44.88	27.62	12.84	11.00	15.80

	CC	0.93	0.98	0.84	0.79	0.67	0.65	0.96	0.99	1.00	1.00
Method-3 (melted)	α_L	1.54	2.33	2.41	2.25	0.99	0.77	1.29	1.05	1.09	1.06
	α_0	0.10	0.08	0.14	0.13	0.19	0.26	0.00	0.04	0.04	0.06
	RMSE	0.27	0.46	0.51	0.51	0.35	0.46	0.26	0.10	0.17	0.23
	MAE	0.13	0.27	0.30	0.28	0.20	0.25	0.11	0.06	0.10	0.16
	MAPE	40.50	49.24	50.27	47.38	46.46	45.30	28.44	15.68	13.54	21.14
	CC	0.79	0.99	0.93	0.87	0.74	0.45	0.93	0.99	0.99	0.99

504

505 **Table A2: Comparison of precipitation intensity based on weighing rain gauge and 2DVD observation data for each T_w range.**

		T1	T2	T3	T4	T5	T6	T7	T8	T9	T10
Unfiltered	α_L	7.36	3.39	3.98	3.86	2.25	2.15	1.37	1.01	1.03	1.03
	α_0	0.09	0.12	0.27	0.09	0.24	0.06	0.04	0.04	0.02	0.01
	RMSE	1.04	0.88	0.95	0.93	0.76	0.64	0.33	0.14	0.12	0.17
	MAE	0.44	0.46	0.57	0.43	0.43	0.31	0.15	0.08	0.07	0.12
	MAPE	49.76	55.42	60.80	48.81	53.44	41.61	41.39	22.03	13.07	19.05
	CC	0.98	0.97	0.90	0.93	0.88	0.89	0.95	0.98	0.99	0.99
Method-1	α_L	0.61	0.26	0.48	0.93	0.48	0.61	1.11	0.97	0.98	0.98
	α_0	0.02	0.03	0.06	0.05	0.09	0.05	0.04	0.05	0.02	0.01
	RMSE	0.13	0.17	0.13	0.19	0.28	0.20	0.20	0.13	0.10	0.14
	MAE	0.06	0.07	0.07	0.12	0.13	0.11	0.10	0.08	0.07	0.10
	MAPE	25.71	63.33	41.35	41.49	36.12	79.17	38.21	22.17	14.21	21.89
	CC	0.70	0.65	0.73	0.80	0.79	0.71	0.96	0.98	0.99	1.00
Method-2	α_L	0.53	0.58	0.21	0.46	0.28	0.80	0.88	0.95	0.94	0.93
	α_0	0.01	0.00	0.01	0.03	0.06	0.01	0.05	0.03	0.03	0.02
	RMSE	0.07	0.03	0.09	0.18	0.31	0.10	0.11	0.12	0.11	0.17
	MAE	0.02	0.01	0.06	0.11	0.15	0.07	0.07	0.07	0.07	0.12
	MAPE	22.22	11.11	28.57	85.56	55.43	27.34	35.56	18.32	14.12	20.69
	CC	0.82	0.94	0.45	0.75	0.78	0.92	0.98	0.98	1.00	1.00
Method-3	α_L	1.91	2.01	2.33	2.02	0.92	1.04	1.12	1.01	1.03	1.03
	α_0	0.07	0.10	0.15	0.10	0.15	0.10	0.05	0.04	0.02	0.01
	RMSE	0.22	0.41	0.52	0.45	0.29	0.21	0.16	0.14	0.12	0.17
	MAE	0.12	0.25	0.29	0.24	0.16	0.13	0.09	0.08	0.07	0.12
	MAPE	42.13	49.58	52.32	44.83	46.50	37.92	34.21	22.03	13.07	19.05
	CC	0.91	0.98	0.86	0.90	0.80	0.90	0.98	0.98	0.99	0.99

Method-1 (melted)	α_x	1.16	0.65	0.89	1.12	0.57	0.79	1.15	0.99	0.99	0.98
	α_a	0.05	0.03	0.09	0.06	0.12	0.06	0.04	0.04	0.02	0.01
	RMSE	0.11	0.13	0.16	0.23	0.26	0.16	0.21	0.13	0.10	0.13
	MAE	0.06	0.08	0.10	0.11	0.15	0.10	0.09	0.08	0.06	0.10
	MAPE	30.25	31.05	36.50	29.44	49.92	32.10	37.80	22.22	13.91	21.50
	CC	0.90	0.97	0.82	0.82	0.77	0.89	0.96	0.98	1.00	1.00
Method-2 (melted)	α_x	0.91	0.53	0.65	0.74	0.38	0.61	0.93	0.96	0.95	0.95
	α_a	0.01	0.02	0.07	0.05	0.09	0.04	0.05	0.04	0.02	0.01
	RMSE	0.04	0.18	0.14	0.17	0.29	0.18	0.09	0.12	0.11	0.15
	MAE	0.01	0.10	0.09	0.11	0.14	0.10	0.06	0.07	0.07	0.11
	MAPE	8.89	35.56	34.62	42.75	58.79	40.35	34.42	17.78	14.24	22.16
	CC	0.98	0.98	0.79	0.82	0.77	0.87	0.99	0.98	1.00	1.00
Method-3 (melted)	α_x	2.24	2.10	2.47	2.08	0.99	1.14	1.13	1.01	1.03	1.03
	α_a	0.07	0.10	0.16	0.11	0.16	0.10	0.05	0.04	0.02	0.01
	RMSE	0.27	0.44	0.55	0.48	0.30	0.22	0.16	0.14	0.12	0.17
	MAE	0.14	0.26	0.32	0.25	0.17	0.14	0.09	0.08	0.07	0.12
	MAPE	43.48	49.81	51.47	45.14	46.83	38.15	37.14	22.03	13.07	19.05
	CC	0.93	0.98	0.86	0.89	0.82	0.92	0.98	0.98	0.99	0.99

506 Table A3: Diameter-channel information of the PARSIVEL disdrometer.

Channel number	Mid-value of channel (mm)	Diameter spread (mm)	Channel number	Mid-value of channel (mm)	Diameter spread (mm)
1	0.062	0.125	17	3.250	0.500
2	0.187	0.125	18	3.750	0.500
3	0.312	0.125	19	4.250	0.500
4	0.437	0.125	20	4.750	0.500
5	0.562	0.125	21	5.500	1.000
6	0.687	0.125	22	6.500	1.000
7	0.812	0.125	23	7.500	1.000
8	0.937	0.125	24	8.500	1.000
9	1.062	0.125	25	9.500	1.000
10	1.187	0.125	26	11.000	2.000
11	1.375	0.250	27	13.000	2.000
12	1.625	0.250	28	15.000	2.000

13	1.875	0.250	29	17.000	2.000
14	2.125	0.250	30	19.000	2.000
15	2.375	0.250	31	21.500	3.000
16	2.750	0.500	32	24.500	3.000

507 **Table A4: Velocity channel information of the PARSELV disdrometer.**

Channel number	Mid-value of channel (mm)	Velocity spread (mm)	Channel number	Mid-value of channel (mm)	Velocity spread (mm)
1	0.050	0.100	17	2.600	0.400
2	0.150	0.100	18	3.000	0.400
3	0.250	0.100	19	3.400	0.400
4	0.350	0.100	20	3.800	0.400
5	0.450	0.100	21	4.400	0.800
6	0.550	0.100	22	5.200	0.800
7	0.650	0.100	23	6.000	0.800
8	0.750	0.100	24	6.800	0.800
9	0.850	0.100	25	7.600	0.800
10	0.950	0.100	26	8.800	1.600
11	1.100	0.200	27	10.400	1.600
12	1.300	0.200	28	12.000	1.600
13	1.500	0.200	29	13.600	1.600
14	1.700	0.200	30	15.200	1.600
15	1.900	0.200	31	17.600	3.200
16	2.200	0.400	32	20.800	3.200

508 **Data availability**

509 The data used in this study are available from the corresponding author upon reasonable request.

510 **Author contributions**

511 HJK and CJ, conceptualized the project. JB did the data curation and formal analysis. HJK and SHS did the analysis and
512 interpretation. HJK and JB led the investigation. HJK prepared the original draft, and SHS and CJ reviewed and edited the
513 paper. All authors have read and agreed to the published version of the paper.

514 **Competing Interests**

515 The contact author has declared that none of the authors has any competing interests.

서식 있음: 표준

516 **Acknowledgements**

517 This study was supported by the Basic Science Research Program through the National Research Foundation of Korea
518 (NRF), funded by the Ministry of Education (RS-2022-NR071182).

519 **Financial support**

520 This study was supported by the Basic Science Research Program through the National Research Foundation of Korea
521 (NRF), funded by the Ministry of Education (RS-2022-NR071182).

522 **Competing Interest**

523 Atlas, D., Srivastava, R. C., and Sekhon, R. S.: Doppler radar characteristics of precipitation at vertical incidence, *Rev.*
524 *Geophys.*, 11, 1–35. <https://doi.org/10.1029/RG011i001p00001>, 1973.

525 Barthazy, E. and Schefold, R.: Fall velocity of snowflakes of different riming degree and crystal types, *Atmos. Res.*, 82,
526 391–398. <https://doi.org/10.1016/j.atmosres.2005.12.009>, 2006.

527 Beard, K. V.: Terminal velocity adjustment for cloud and precipitation drops aloft, *J. Atmos. Sci.*, 34, 1293–1298.
528 [https://doi.org/10.1175/1520-0469\(1977\)034<1293:TVAFCA>2.0.CO;2](https://doi.org/10.1175/1520-0469(1977)034<1293:TVAFCA>2.0.CO;2), 1977.

529 Brandes, E. A., Zhang, G., and Vivekanandan, J.: Experiments in rainfall estimation with a polarimetric radar in a
530 subtropical environment, *J. Appl. Meteor.*, 41, 674–685. [https://doi.org/10.1175/1520-0450\(2002\)041<0674:EIREWA>2.0.CO;2](https://doi.org/10.1175/1520-0450(2002)041<0674:EIREWA>2.0.CO;2), 2002.

532 Chang, W. Y., Wang, T. C. C., and Lin, P. L.: Characteristics of the raindrop size distribution and drop shape relation in
533 typhoon systems in the western Pacific from the 2D video disdrometer and NCU C-band polarimetric radar, *J. Atmos.*
534 *Ocean. Technol.*, 26, 1973–1993. <https://doi.org/10.1175/2009JTECHA1236.1>, 2009.

535 Dahlström, B.: Cloud physical and climatological factors for the determination of rain intensity, *Water*, 13, 2292.
536 <https://doi.org/10.3390/w13162292>, 2021.

537 Delanoë, J., Protat, A., Testud, J., Bouniol, D., Heymsfield, A. J., Bansemmer, A., Brown, P. R. A., Forbes, R. M.: Statistical
538 properties of the normalized ice particle size distribution, *J. Geophys. Res. Atmos.*, 110.
539 <https://doi.org/10.1029/2004JD005405>, 2005.

540 Deo, A. and Walsh, K. J. E.: Contrasting tropical cyclone and non-tropical cyclone related rainfall drop size distribution at
541 Darwin, Australia, *Atmos. Res.*, 181, 81–94. <https://doi.org/10.1016/j.atmosres.2016.06.015>, 2016.

542 Ding, B., Yang, K., Qin, J., Wang, L., Chen, Y., and He, X.: The dependence of precipitation types on surface elevation and
543 meteorological conditions and its parameterization, *J. Hydrol.*, 513, 154–163.
544 <https://doi.org/10.1016/j.jhydrol.2014.03.038>, 2014.

545 Du, Y. and Chen, G.: Heavy rainfall associated with double low-level jets over southern China. Part II: Convection initiation,
546 *Mon. Weather Rev.*, 147, 543–565. <https://doi.org/10.1175/MWR-D-18-0102.1>, 2019.

547 Friedrich, K., Kalina, E. A., Masters, F. J., and Lopez, C. R.: Drop-size distributions in thunderstorms measured by optical
548 disdrometers during VORTEX2, *Mon. Weather Rev.*, 141, 1182–1203. <https://doi.org/10.1175/MWR-D-12-00116.1>,
549 2013.

550 Gong, Y., He, T., Chen, M., Wang, B., Nie, L., and Yin, Y.: Spatio-temporal enhanced contrastive and contextual learning
551 for weather forecasting, *IEEE Trans. Knowl. Data Eng.*, 36, 4260–4274. <https://doi.org/10.1109/TKDE.2024.3362825>,
552 2024.

553 Grazioli, J., Tuia, D., Monhart, S., Schneebeli, M., Raupach, T., and Berne, A.: Hydrometeor classification from two-
554 dimensional video disdrometer data, *Atmos. Meas. Tech.*, 7, 2869–2882. <https://doi.org/10.5194/amt-7-2869-2014>,
555 2014.

556 Guo, J., Liu, H., Li, Z., Rosenfeld, D., Jiang, M., Xu, W., Jiang, J. H., He, J., Chen, D., Min, M., Zhai, P.: Aerosol-induced
557 changes in the vertical structure of precipitation: A perspective of TRMM precipitation radar, *Atmos. Chem. Phys.*, 18,
558 13329–13343. <https://doi.org/10.5194/acp-18-13329-2018>, 2018.

559 Hu, A. Z. and Igel, A. L.: A bin and a bulk microphysics scheme can be more alike than two bin schemes, *J. Adv. Model.*
560 *Earth Syst.*, 15, MS003303, e2022. <https://doi.org/10.1029/2022MS003303>, 2023.

561 Insel, N., Poulsen, C. J., and Ehlers, T. A.: Influence of the Andes Mountains on South American moisture transport,
562 convection, and precipitation, *Clim. Dyn.*, 35, 1477–1492. <https://doi.org/10.1007/s00382-009-0637-1>, 2010.

563 Iversen, E. C., Thompson, G., and Nygaard, B. E.: Improvements to melting snow behavior in a bulk microphysics scheme,
564 *Atmos. Res.*, 253, 105471. <https://doi.org/10.1016/j.atmosres.2021.105471>, 2021.

565 Jaffrain, J. and Berne, A.: Experimental quantification of the sampling uncertainty associated with measurements from
566 PARSIVEL disdrometers, *J. Hydrol. Meteorol.*, 12, 352–370. <https://doi.org/10.1175/2010JHM1244.1>, 2011.

567 Ji, L., Chen, H., Li, L., Chen, B., Xiao, X., Chen, M., and Zhang, G.: Raindrop size distributions and rain characteristics
568 observed by a PARSIVEL disdrometer in Beijing, Northern China, *Remote Sens.*, 11, 1479.
569 <https://doi.org/10.3390/rs11121479>, 2019.

570 Kim, H. J., Jung, W., Suh, S. H., Lee, D. I., and You, C. H.: The characteristics of raindrop size distribution at windward and
571 leeward side over mountain area, *Remote Sens.*, 14, 2419. <https://doi.org/10.3390/rs14102419>, 2022.

572 Kim, H. J., Lee, K. O., You, C. H., Uyeda, H., and Lee, D. I.: Microphysical characteristics of a convective precipitation
573 system observed on July 04, 2012, over Mt. Halla in South Korea, *Atmos. Res.*, 222, 74–87.
574 <https://doi.org/10.1016/j.atmosres.2019.02.011>, 2019.

575 Kochendorfer, J., Earle, M. E., Hodyss, D., Reverdin, A., Roulet, Y. A., Nitu, R., Rasmussen, R., Landolt, S., Buisán, S.,
576 Laine, T.: Undercatch adjustments for tipping-bucket gauge measurements of solid precipitation, *J. Hydrol. Meteorol.*,
577 21, 1193–1205. <https://doi.org/10.1175/JHM-D-19-0256.1>, 2020.

578 Kruger, A. and Krajewski, W. F.: Two-dimensional video disdrometer: A description, *J. Atmos. Ocean. Technol.*, 19, 602–
579 617. [https://doi.org/10.1175/1520-0426\(2002\)019<0602:TDVDAD>2.0.CO;2](https://doi.org/10.1175/1520-0426(2002)019<0602:TDVDAD>2.0.CO;2), 2002.

580 Lee, K. O., Uyeda, H., and Lee, D. I.: Microphysical structures associated with enhancement of convective cells over Mt.
581 Halla, Jeju Island, Korea on 6 July 2007, *Atmos. Res.*, 135–136, 76–90.
582 <https://doi.org/10.1016/j.atmosres.2013.08.012>, 2014.

583 Lintner, B. R., Adams, D. K., Schiro, K. A., Stansfield, A. M., Amorim Rocha, A. A., and Neelin, J. D.: Relationships
584 among climatological vertical moisture structure, column water vapor, and precipitation over the central Amazon in
585 observations and CMIP5 models, *Geophys. Res. Lett.*, 44, 1981–1989. <https://doi.org/10.1002/2016GL071923>, 2017.

586 Liu, X., Li, H., Hu, S., Wan, Q., Xiao, H., Zheng, T., Li, M., Ye, L., Guo, Z., Wang, Y., Yan, Z.: A high-precision and fast
587 solution method of gamma raindrop size distribution based on 0-moment and 3-moment in South China, *J. Appl.*
588 *Meteorol. Climatol.*, 60, 1407–1421. <https://doi.org/10.1175/JAMC-D-21-0043.1>, 2021.

589 Lu, Y., Yu, Z., Albertson, J. D., Chen, H., Hu, L., Pendergrass, A., Chen, X., Li, Q.: Understanding the influence of urban
590 form on the spatial pattern of precipitation, *Earths Future*, 12, EF003846, e2023.
591 <https://doi.org/10.1029/2023EF003846>, 2024.

592 Maheskumar, R. S., Padmakumari, B., Konwar, M., Morwal, S. B., and Deshpande, C. G.: Characterization of hydrometeors
593 and precipitation over the Indian monsoon region using aircraft measurements, *Atmos. Res.*, 205, 147–154.
594 <https://doi.org/10.1016/j.atmosres.2018.02.012>, 2018.

595 Marshall, J. S. and Palmer, W. M. K.: The distribution of raindrops with size, *J. Atmos. Sci.*, 5, 165–166.
596 [https://doi.org/10.1175/1520-0469\(1948\)005<0165:TDORWS.2.0.CO;2](https://doi.org/10.1175/1520-0469(1948)005<0165:TDORWS.2.0.CO;2), 1948.

597 Marzuki, M., Randeu, W. L., Schönhuber, M., Bringi, V. N., Kozu, T., and Shimomai, T.: Raindrop size distribution
598 parameters of distrometer data with different bin sizes, *IEEE Trans. Geosci. Remote Sens.*, 48, 3075–3080.
599 <https://doi.org/10.1109/TGRS.2010.2043955>, 2010.

600 Ong, C. R., Miura, H., Koike, M.: The terminal velocity of axisymmetric cloud drops and raindrops evaluated by the
601 immersed boundary method. *J. Atmos Sci.*, 78(4), 1129–1146. <https://doi.org/10.1175/JAS-D-20-0161.1>, 2021.

602 Padullés, R., Kuo, Y. H., Neelin, J. D., Turk, F. J., Ao, C. O., and De la Torre Juárez, M.: Global tropical precipitation
603 relationships to free-tropospheric water vapor using radio occultations, *J. Atmos. Sci.*, 79, 1585–1600.
604 <https://doi.org/10.1175/JAS-D-21-0052.1>, 2022.

605 Raupach, T. H. and Berne, A.: Correction of raindrop size distributions measured by Parsivel disdrometers, using a two-
606 dimensional video disdrometer as a reference, *Atmos. Meas. Tech.*, 8, 343–365. [https://doi.org/10.5194/amt-8-343-](https://doi.org/10.5194/amt-8-343-2015)
607 [2015](https://doi.org/10.5194/amt-8-343-2015), 2015.

608 Savina, M., Schäppi, B., Molnar, P., Burlando, P., and Sevruk, B.: Comparison of a tipping-bucket and electronic weighing
609 precipitation gage for snowfall, *Atmos. Res.*, 103, 45–51. <https://doi.org/10.1016/j.atmosres.2011.06.010>, 2012.

610 Segovia-Cardozo, D. A., Rodríguez-Sinobas, L., Díez-Herrero, A., Zobelzu, S., and Canales-Ide, F.: Understanding the
611 mechanical biases of tipping-bucket rain gauges: A semi-analytical calibration approach, *Water*, 13, 2285.
612 <https://doi.org/10.3390/w13162285>, 2021.

613 Serio, M. A., Carollo, F. G., and Ferro, V.: Raindrop size distribution and terminal velocity for rainfall erosivity studies. A
614 review, *J. Hydrol.*, 576, 210–228. <https://doi.org/10.1016/j.jhydrol.2019.06.040>, 2019.

615 Smith, P. L.: Raindrop size distributions: Exponential or gamma—Does the difference matter?, *J. Appl. Meteor.*, 42, 1031–
616 1034. [https://doi.org/10.1175/1520-0450\(2003\)042<1031:RSDEOG>2.0.CO;2](https://doi.org/10.1175/1520-0450(2003)042<1031:RSDEOG>2.0.CO;2), 2003.

617 Steenburgh, W. J.: Sea-effect precipitation: A Look at Japan’s “Gosetsu Chitai”, *Bull. Am. Meteorol. Soc.*, 101, 129–136.
618 <https://doi.org/10.1175/BAMS-D-18-0335.A>, 2020.

619 Stull, R.: Wet-bulb temperature from relative humidity and air temperature, *J. Appl. Meteorol. Climatol.*, 50, 2267–2269.
620 <https://doi.org/10.1175/JAMC-D-11-0143.1>, 2011.

621 Syпка, P.: Dynamic real-time volumetric correction for tipping-bucket rain gauges, *Agric. Forest Meteorol.*, 271, 158–167.
622 <https://doi.org/10.1016/j.agrformet.2019.02.044>, 2019.

623 Tang, Y. S., Chang, P. L., Chang, W. Y., Zhang, J., Tang, L., Lin, P. F., and Chen, C. R.: A localized quantitative
624 precipitation estimation for S-band polarimetric radar in Taiwan, *J. Hydrol. Meteorol.*, 25, 1697–1712.
625 <https://doi.org/10.1175/JHM-D-23-0205.1>, 2024.

626 Thomas, A., Kanawade, V. P., Chakravarty, K., and Srivastava, A. K.: Characterization of raindrop size distributions and its
627 response to cloud microphysical properties, *Atmos. Res.*, 249, 105292.
628 <https://doi.org/10.1016/j.atmosres.2020.105292>, 2021.

629 Thurai, M. and Bringi, V. N.: Drop axis ratios from a 2D video disdrometer, *J. Atmos. Ocean. Technol.*, 22, 966–978.
630 <https://doi.org/10.1175/JTECH1767.1>, 2005.

631 Tiira, J., Moisseev, D. N., Von Lerber, A., Ori, D., Tokay, A., Bliven, L. F., and Petersen, W.: Ensemble mean density and
632 its connection to other microphysical properties of falling snow as observed in Southern Finland, *Atmos. Meas. Tech.*,
633 9, 4825–4841. <https://doi.org/10.5194/amt-9-4825-2016>, 2016.

634 Ulbrich, C. W.: Natural variations in the analytical form of the raindrop size distribution, *J. Clim. Appl. Meteorol.*, 22, 1764–
635 1775. [https://doi.org/10.1175/1520-0450\(1983\)022<1764:NVITAF>2.0.CO;2](https://doi.org/10.1175/1520-0450(1983)022<1764:NVITAF>2.0.CO;2), 1983.

636 Vázquez-Martín, S., Kuhn, T., and Eliasson, S.: Mass of different snow crystal shapes derived from fall speed measurements,
637 *Atmos. Chem. Phys.*, 21, 18669–18688. <https://doi.org/10.5194/acp-21-18669-2021>, 2021.

638 Wang, P. K. and Pruppacher, H. R.: Acceleration to terminal velocity of cloud and raindrops. *J. Appl. Meteorol. Clim.*, 16(3),
639 275–280. [https://doi.org/10.1175/1520-0450\(1977\)016<0275:ATTVOC>2.0.CO;2](https://doi.org/10.1175/1520-0450(1977)016<0275:ATTVOC>2.0.CO;2), 1977.

640 Wen, L., Zhao, K., Chen, G., Wang, M., Zhou, B., Huang, H., Hu, D., Lee, W. C., Hu, H.: Drop size distribution
641 characteristics of seven typhoons in China, *J. Geophys. Res. Atmos.*, 123, 6529–6548.
642 <https://doi.org/10.1029/2017JD027950>, 2018.

643 Yang, Q., Dai, Q., Han, D., Chen, Y., and Zhang, S.: Sensitivity analysis of raindrop size distribution parameterizations in
644 WRF rainfall simulation, *Atmos. Res.*, 228, 1–13. <https://doi.org/10.1016/j.atmosres.2019.05.019>, 2019.

645 Yang, Y., Wang, R., Chen, F., Liu, C., Bi, X., and Huang, M.: Synoptic weather patterns modulate the frequency, type and
646 vertical structure of summer precipitation over Eastern China: A perspective from GPM observations, *Atmos. Res.*, 249,
647 105342. <https://doi.org/10.1016/j.atmosres.2020.105342>, 2021.

648 Yao, X., Yang, K., Zhou, X., Wang, Y., Lazhu, C., Chen, Y., and Lu, H.: Surface friction contrast between water body and
649 land enhances precipitation downwind of a large lake in Tibet, *Clim. Dyn.*, 56, 2113–2126.
650 <https://doi.org/10.1007/s00382-020-05575-x>, 2021.

651 Yi, Y., Yi, F., Liu, F., Zhang, Y., Yu, C., and He, Y.: Microphysical process of precipitating hydrometeors from warm-front
652 mid-level stratiform clouds revealed by ground-based lidar observations, *Atmos. Chem. Phys.*, 21, 17649–17664.
653 <https://doi.org/10.5194/acp-21-17649-2021>, 2021.

654